Heliyon 10 (2024) e26464

Contents lists available at ScienceDirect

Heliyon

journal homepage: www.cell.com/heliyon

Review article

Development of high entropy alloys (HEAs): Current trends

Balaji V [a], Anthony Xavior M [a,*]

[a] School of Mechanical Engineering, Vellore Institute of Technology, Vellore 632 014, Tamil Nadu, India

ARTICLE INFO

Keywords:
High entropy alloys (HEAs)
High entropy effect
Phase formation
Physical metallurgy

ABSTRACT

A novel concept of developing multi-principal elements, or compositional complex alloys is referred as high-entropy alloys (HEAs). This review addresses the role of entropy in alloying additions along with the effect of various elements listed in the periodic table in forming the HEAs. Phase formation rules and the associated parameters along with their significance are discussed. The physical metallurgy technique is elaborated with reference to the high-entropy effect, severe lattice distortion effect, sluggish diffusion effect, and cocktail effects. Various types of HEAs such as light weight HEAs, nanoprecipitate HEAs, ultrafine-grained HEAs, dual-phase HEAS and TRIP/TWIN HEAs are discussed. Further, the effects of mechanical alloying in HEAs are presented. Finally, the microstructural effects and mechanical properties of HEAs are addressed with reference to the published literature.

1. Introduction

This review article addresses the recent trends in the development of high-entropy alloys (HEAs) and their properties and applications based on powder metallurgical processes. The combination of several elements addition and their property evaluation is a current industry expectation because of, to improve simultaneously improvement mechanical properties. Like improving the hardness as well as improving the ductility. From the industrial perspective, newer ones have lower costs and better performance than older ones. In this direction, researchers have developed materials with different combinations referred to as HEAs, which were also called compositional complex alloys (CCAs) and multi-principle component alloys (MCAs) [1]. The formation of HEAs is based on various alloy-forming rules and HEAs effects. HEAs consider five or more than five principal block elements between 5 and 35 atomic percentages (at. %). Ranges with equal or near-equal atomic combinations in homogeneous or heterogeneous mixing are possible. The alloy's ability and performance are based on its defect-free nature based on homogenous and heterogenous structures [2,3]. This way of HEAs production has a lower cost than titanium and super alloys but is still higher than light-weight Al alloys and steels [4].

In the future, the focus of material science will be on light-weight materials because of more energy savings and reduced Co_2 emissions. A density $\leq 5\ g/cm^3$ called light-weight HEAs (LWHEAs). Based on fabrication methods the value of density varies. The light-weight material enhancement elements like Li, Rb, Mg, Al, Sc, Ba, Y, and Ti are widely used by various researchers. Work on light-weight elements like $Al_{14}Li_{11}Mg_{35}Ti_{15}Zr_{25}$ alloy is focused on achieving a density of 3.36 g/cm^3 for aerospace applications. $Al_{20}Be_{20}Fe_{10}Si_{15}Ti_{35}$ density of 3.91 g/cm^3 for high-temperature applications [5]. $C_{0.38}Mn_{6.74}Si_{1.27}Al_{2.91}V_{0.38}Nb_{0.034}B_{0.0029}$ (wt. %) in the high concentration of Al and Si reduces the weight density between 7.8 g/cm^3 changes to 7.39 g/cm^3 [6]. In all the categories of HEAs, the density value lies between 3 and 11.49 g/cm^3. LWHEAs represent 3 to 6 times higher hardness than conventional AZ31 alloys. The fracture behavior of HEAs is strain rate <5% for this HEAs material that is less susceptible. Which can enhance the higher,

* Corresponding author.
E-mail address: manthonyxavior@vit.ac.in (A.X. M).

https://doi.org/10.1016/j.heliyon.2024.e26464
Received 29 November 2023; Received in revised form 13 February 2024; Accepted 14 February 2024
Available online 19 February 2024

more complex conditions. The addition of reinforcement, heat treatment, and enhanced hardness from preparation methods all contribute to lowering this strain rate [7]. Subsequently, it forms a nanoprecipitation with the help of heat treatment to reduce/impede the dislocation motion. The nanoparticles needed to make a top-down approach are preferable because of the miniaturizing material usage. Adding reinforcement like graphene is the essential structural element of carbon allotropes, including graphite, carbon nanotubes, and fullerenes. It can conduct electrons and is transparent [8]. $Fe_{40}Co_{30}Mn_{15}Al_{15}$ elements have excellent soft magnetic performance for electrical applications like electrical machines. The ordered B_2-phase enhances the Co/Al addition, which helps to increase HEAs hardness. Uniformly distributed BCC-structured nanoprecipitates improve resistance to fracture and softening at high temperatures with the addition of Fe/Mn in HEAs and appealing tribological qualities [9]. Hardness primarily depends on the type of structure, like homogenous and heterogenous; mechanical alloying is an essential process for forming homogenous mixing of solid solution strengthening. Moreover, they add a small amount of alloying additions Fe and Co to stifle the diffusion rate. The valence electron concentration (VEC) forms the basis for predicting face evaluation. Based on face evaluation, crystal structures like BCC, FCC, HCP, and intermetallic phase are identified in a particular alloy system [10]. The alloy system of AlMgZnCuMn forms without excessive intermetallic compound formation. The effects of high-temperature materials not used for cycle or impact loading affected the entropy levels. High mixing entropy results in HEAs having a higher solid solution stability [11]. With the help of mechanical alloying to enhance the solid solution stability, increasing the mechanical alloying time, reducing the density, and finally, the element behavior changed BCC or FCC or intermetallic phase structure. Milling time is one of the influencing factors for the change of crystal structure of alloys. Addition of Al-based HEAs up to 30 h as BCC to FCC phases are present. No other intermetallic phases are identified in the AlFeCuNiMgZn HEAs system [12]. Among the process control agents (PCAs) added to improve mechanical alloying to reduce contamination and improve the cold fraction. These are toluene, methanol, benzene, ethyl acetate, and N-heptane. The PCAs prevent the heating effect during the mechanical collision during mechanical alloying for a prolonged duration and act as good surface agents [13]. The ball-to-powder ratio is one of the parameters for changing the particle size to make a fine powder with a lower economic mode [14]. Effects of addition, more amount of Ni to the $Fe_{20}Co_{20}Ni_{41}Al_{19}$ HEAs system to form a nano-lamellar eutectic microstructure, with a temperature of 1100 $^{\circ}C$, h as tensile strength, and the total elongation increase up to 1103 MPa and 18.7% [15]. Increase the major and significant difference between BCC crystal structures compared to FCC. BCC structure has higher strength, good corrosion resistance, and lower plasticity. At the same time, HEAs of the FCC structure have higher plasticity and lower strength [15]. After the various particle size distributions as measured by the laser diffraction approach. ASTM B311-13 was used to measure the sample's density in the form of a powder metallurgy route with the help of the Archimedes principle with <2 % level of porosity [16]. Metal powder particles with coarse structures represent the highest density and low resistance against compaction pressure [17]. Comparing different sintering techniques, such as high-frequency induction heat sintering (HFIHS) and conventional sintering (CS), the CS is 80%, and HFIHS is 95% of the final density achieved. Higher densification to achieve higher mechanical properties [18]. Mechanical alloying of nanomaterial synthesis plays an essential role in the M_2AX phase on 2D counterparts. M_2AX phase stability depends on Ti and V. In M_2AX phases, increasing the VEC does not affect the density of the given state [19]. The configurational entropy rises in thermodynamic criteria based on HEAs as the number of elements does [20]. One noticeable advantage of HEAs is that they reduce the diffusion rate with improved lattice distortion, which results in enhanced high-temperature stability [21]. FCC + L_{12} phases reduced the strain accumulated from dislocation shear and prevented the crack initiation. Nanoprecipitation forms during the heat treatment process. Annealing at a high temperature does not result in coarse grain formation, whereas it forms fine grains [22]. Medical applications of hafnium (Hf) in bio-HEAs are significant, and Hf contributes to lower magnetic sustainability, which is suitable for MRI carriers [23].

Following the fabrication procedures, material characterization including hardness, wear behavior, corrosion, and nano-indentation measurements is used to determine whether or not to produce HEAs for a certain application. The valence electron concentration and the variation in atomic size different play a vital role in defining the hardness of the HEAs. Monotonously increasing the hardness between the VEC of 6.5–7.0. Atomic size difference is 6%. Subsequently, the monophase structure is also advantageous for enhancing hardness. The mono-phase structure prevents the distortion effect and minimizes dislocation motion [24]. Followed by various process conditions like As-rolled (hot and cold rolling), As-annealed, and As-homogenized conditions are used to improve the hardness. From those conditions, As- rolled (hot and cold) to achieve the highest hardness in the $Al_{0.5}CoCrCuFeNi$ HEAs system. The As-cast condition to improve the hardness using various processes like As-rolled, As-annealed, and As-homogenized conditions are used to improve the hardness. From those conditions, As- rolled (hot and cold) to achieve the highest hardness in the $Al_{0.5}CoCrCuFeNi$ HEAs system [25]. Fabrication of copper-based HEAs with the addition of Al to the Cu most wear resistance with fine grain

Table 1
Entropy values for various entropy alloys [7].

Low entropy alloy	Medium entropy alloy	High entropy alloy
$\triangle S \leq 1.0R$ 1 or 2 Principal elements. Solid solution and Intermetallic compounds to form.	$1.0R \leq \triangle S \leq 1.5R$ 2 to 4 Principal elements.	$\triangle S \geq 1.5R$ At least 5 Principal elements. Single-phase solid solution – disordered or partially ordered to form.

The low, medium, and high entropy values should be used appropriately to modify the microstructure and depart from the equiatomic combination. Low entropy alloys have non-equiatomic combinations, so multiphase microstructure development occurs. A multiphase microstructure develops by incorporating equiatomic and non-equiatomic elements into medium entropy alloys. Single-phase or multiphase microstructures are formed by high entropy alloys, including equiatomic and non-equiatomic phases [27].

Table 2
List of Elements and the values for the corresponding parameters.

AN	E	EN_1	Density g/cm^3	Y-modulus	Melting point (°C)	Boiling point (°C)	Atomic size (nm)	VEC	EN_1 (P-scale)	Atomic mass	Crystal structure
1	H	Hydrogen	0.00008	–	−259.2	−252.7	0.154	1	2.2	1.008	–
2	He	Helium	0.000168	–	–	−268.9	0.05	2	–	4.003	–
3	Li	Lithium	0.534	4.9	180.5	1342	0.152	1	0.98	6.94	BCC
4	Be	Beryllium	1.85	287	1287	2468	0.114	2	1.57	9.012	HCP
5	B	Boron	2.34	–	2077	4000	0.088	3	2.04	10.81	Rhomb
6	C	Carbon	2.25	–	3825	3825	0.0701	4	2.55	12.011	Hex
7	N	Nitrogen	0.001	–	−209.9	−195.8	0.070	5	3.04	14.007	–
8	O	Oxygen	0.0013	–	−218.8	−183.0	0.066	6	3.44	15.990	–
9	F	Fluorine	0.0015	–	−220	−188.1	0.064	7	3.98	18.998	–
10	Ne	Neon	0.0009	10	−248.7	−246.0	0.070	8	–	20.18	–
11	Na	Sodium	0.971		97.79	882.9	0.186	1	0.93	22.99	BCC
12	Mg	Magnesium	1.74	45	649	1090	0.160	2	1.31	24.31	HCP
13	Al	Aluminium	2.702	70	660.4	2519	0.143	3	1.61	26.98	FCC
14	Si	Silicon	2.33	47	1414	3265	0.118	4	1.90	28.08	Dia Cubic
15	P	Phosphorus	1.82	–	44.15	280	0.109	5	2.19	30.97	Ortho
16	S	Sulfur	2.07	–	115.2	444.6	0.106	6	2.58	32.06	Ortho
17	Cl	Chlorine	0.002	–	−101.0	−34.0	–	7	3.16	35.45	–
18	Ar	Argon	0.0016	–	−189.2	−185.8	–	8	–	39.95	–
19	K	Potassium	0.862	–	63	759	0.231	1	0.82	39.09	BCC
20	Ca	Calcium	1.55	20	842	1484	0.197	2	1.00	40.07	FCC
21	Sc	Scandium	2.99	74	1541	2836	–	3	1.36	44.95	–
22	Ti	Titanium	4.51	116	1670	3287	0.145	4	1.54	47.86	HCP
23	V	Vanadim	6.0	128	1910	3407	0.132	5	1.63	50.94	BCC
24	Cr	Chromium	7.15	279	1907	2671	0.125	6	1.66	51.99	BCC
25	Mn	Manganese	7.3	198	1246	2061	0.126	7	1.55	54.94	Cubic
26	Fe	Iron	7.87	211	1538	2861	0.124	8	1.83	55.85	BCC
27	Co	Cobalt	8.86	209	1495	2927	0.125	9	1.88	58.93	HCP
28	Ni	Nickel	8.9	200	1455	2913	0.125	10	1.91	58.69	FCC
29	Cu	Copper	8.96	130	1085	2560	0.128	11	1.90	63.54	FCC
30	Zn	Zinc	7.13	108	420	907	0.133	12	1.65	65.31	HCP
31	Ga	Gallium	5.90	–	29.8	2229	0.122	3	1.81	69.72	Ortho
32	Ge	Germanium	5.323	–	937	2833	0.122	4	2.01	72.64	Dia cubic
33	As	Arsenic	5.75	81	616	616	0.121	5	2.18	74.922	–
34	Se	Selenium	4.809	10	220	685	–	6	2.55	78.97	–
35	Br	Bromine	3.119	–	−7.2	58.78	–	7	2.96	79.90	–
36	Kr	Krypton	0.0034	–	−157	−153	–	8	–	83.798	–
37	Rb	Rubidium	1.53	2.4	39.30	688	–	1	0.82	85.468	–
38	Sr	Strontium	2.64	–	777	1377	–	2	0.95	87.62	–
39	Y	Yttrium	4.47	64	1522	3345	–	3	1.2	88.90	–
40	Zr	Zirconium	6.51	68	1854	4406	0.159	4	1.33	91.22	HCP
41	Nb	Niobium	8.57	105	2477	4741	0.143	5	1.6	92.91	BCC
42	Mo	Molybdenm	10.22	329	2622	4639	0.136	6	2.16	95.95	BCC
43	Tc	Technetium	11	–	2157	4262	–	7	2.10	98.00	–
44	Ru	Ruthenium	12.1	447	2333	4147	–	8	2.2	101.07	–
45	Rh	Rhodium	12.4	275	1963	3695	–	9	2.2	102.90	–
46	Pd	Palladium	12.02	121	1554	2963	–	10	2.2	106.42	–
47	Ag	Silver	10.49	83	961	2162	0.144	11	1.93	107.87	FCC
48	Cd	Cadmium	8.69	50	321	767	0.149	12	1.69	112.41	HCP
49	In	Indium	7.31	11	156.6	2027	–	3	1.78	114.81	–
50	Sn	Tin	7.27	50	231.9	2586	0.151	4	1.96	118.71	Tetra
51	Sb	Antimony	6.68	55	630.5	1587	–	5	2.05	121.76	–
52	Te	Tellurium	6.24	43	450	988	–	6	2.10	127.60	–
53	I	Iodine	4.93	–	113.7	184.35	0.136	7	2.66	126.91	Ortho
54	Xe	Xenon	0.0053	–	−111.9	−108	–	8	2.60	131.29	–
55	Cs	Cesium	1.87	1.71	28.4	671	0.265	1	0.79	132.91	BCC
56	Ba	Barium	3.62	13	727	1845	0.217	2	0.89	137.33	BCC
57	La	Lanthanum	6.15	37	920	3464	–	3	1.10	138.90	–
58	Ce	Cerium	6.77	34	799	3443	–	4	1.12	140.11	–
59	Pr	Praseodymium	6.77	37	931	3520	–	7	1.13	140.90	–
60	Nd	Neodymium	7.01	41	1016	3074	–	6	1.14	144.24	–
61	Pm	Promethium	7.26	–	1042	3000	–	7	–	145.00	–
62	Sm	Samarium	7.52	50	1072	1794	–	8	1.17	150.36	–
63	Eu	Europium	5.24	18	822	1529	–	9	–		–
64	Gd	Gadolinium	7.895	55	1313	3273	–	10	1.20	157.25	–
65	Tb	Terbium	8.23	56	1359	3230	–	11	–	158.92	–
66	Dy	Dysprosium	8.536	61	1412	2567	–	12	1.	162.50	–
67	Ho	Holmium	8.80	65	1472	2700	–	13	1.23	164.93	–

(*continued on next page*)

Table 2 (*continued*)

AN	E	EN_1	Density g/cm^3	Y-modulus	Melting point (°C)	Boiling point (°C)	Atomic size (nm)	VEC	EN_1 (P-scale)	Atomic mass	Crystal structure
68	Er	Erbium	9.05	70	1529	2868	–	14	1.24	167.25	–
69	Tm	Thulium	9.33	74	1545	1950	–	15	1.25	168.93	–
70	Yb	ytterbium	6.90	24	824	1196	–	16	–	173.04	–
71	Lu	Lutetium	9.85	69	1652	3327	–	3	1.2		–
72	Hf	Hafnium	13.3	78	2233	4600	–	4	1.3	178.48	–
73	Ta	Tantalum	16.40	186	3017	5455	–	5	1.5	180.9	–
74	W	Tungsten	19.3	411	3414	5555	0.137	6	1.7	183.84	BCC
75	Re	Rhenium	20.8	463	3185	5590	–	7	1.9	186.20	–
76	Os	Osmium	22.58	–	3033	5008	–	8	2.2	190.23	–
77	Ir	Iridium	22.56	528	2446	4428	–	9	2.2	192.21	–
78	Pt	Platinum	21.50	168	1768	3825	0.139	10	2.2	195.08	FCC
79	Au	Gold	19.32	78	1064	2836	0.144	11	2.4	196.97	FCC
80	Hg	Mercury	13.54	–	−38.80	356.9	–	12	1.9	200.59	–
81	Tl	Thallium	11.85	8	304	1473	–	3	1.8	204.38	–
82	Pb	Lead	11.35	16	327	1749	0.175	4	1.8	207.2	FCC
83	Bi	Bismuth	9.79	32	271.3	1564	–	5	1.9	208.9	–
84	Po	Polonium	9.20	–	254	962	–	6	2.01	209.0	–
85	At	Astatine	–	–	300	350	–	7	2.2	210	–
86	Rn	Radon	0.009	–	−71	−61.8	–	8	–	222.0	–
87	Fr	Francium	–	–	21	650	–	1	0.7	223	–
88	Ra	Radium	5.0	–	696	1500	–	2	0.9	226	–
89	Ac	Actinium	10	–	1050	3200	–	3	1.1	227	–
90	Th	Thorium	11.7	–	1750	4785	–	4	1.3	232.0	–
91	Pa	Protactinium	15.4	–	1572	4000	–	5	1.5	231.03	–
92	U	Uranium	19.1	–	1135	4131	–	6	1.7	238.02	–
93	Np	Neptunium	20.2	–	644	3902	–	7	1.3	237.00	–
94	Pu	Plutonium	19.7	–	640	3228	–	8	1.3	244	–
95	Am	Americium	12	–	1176	2011	–	9	–	243	–
96	Cm	Curium	13.51	–	1345	–	–	10	–	247	–
97	Bk	Berkelium	14.78	–	986	–	–	11	–	247	–
98	Cf	Californium	15.1	–	900	–	–	12	–	251	–
99	Es	Einsteinium	–	–	860	–	–	13	–	252	–
100	Fm	Fermium	–	–	1527	–	–	14	–	257	–
101	Md	Mendelevium	–	–	827	–	–	15	–	258	–
102	No	Nobelium		–	827		–	16	–	259	–
103	Lr	Lawrencium	–	–	1627	–	–	3	–	262	–
104	Rf	Rutherfordium	–	–	–	–	–	4	–	267	–
105	Db	Dubnium	–	–	–	–	–	5	–	268	–
106	Sg	Seaborgium	–	–	–	–	–	6	–	269	–
107	Bh	Bohrium	–	–	–	–	–	7	–	270	–
108	Hs	Hassium	–	–	–	–	–	8	–	269	
109	Mt	Meitnerium	–	–	–	–	–	9	–	278	–
110	Ds	Darmstadtium	–	–	–	–	–	10	–	281	–
111	Rg	Roentgenium	–	–	–	–	–	11	–	280	–
112	Cn	Copernicium	–	–	–	–	–	12	–	285	–
113	Nh	Nihonium	–	–	–	–	–	3	–	286	–
114	Fl	Flerovium	–	–	–	–	–	4	–	289	–
115	Mc	Moscovium	–	–	–	–	–	5	–	289	–
116	Lv	Livermorium	–	–	–	–	–	6	–	293	–
117	Ts	Tennessine	–	–	–	–	–	7	–	294	–
118	Og	oganesson	–	–	–	–	–	8	–	294	–

microstructure and nano precipitations, heat treatments, and solid solution phases to enhance the wear resistance behavior [26]. The mechanical behavior of HEAS to measure with the help of the nanoindentation that effect is briefly explained in the mechanical property section of this paper.

2. Effects of elements in entropy of HEAs

In the HEAs alloy system, the entropy values increase as the principal element addition increases. Table 1 shows that the entropy values vary at low, medium, and high entropy alloys based on significant element additions.

2.1. Elements nature

Formation of various High Entropy Alloys is based on Hume – Rothery rules which are based on certain quantitative parameters like atomic size difference, valency, electronegativity, density, Young's modulus, melting and boiling points, and also the crystal structure. The numerical values of those parameters for each element are presented in Table 2 [28].

3. Effect of various elements in a periodic table

3.1. Alkali metals

Alkali metals comprise group 1 elements (other than hydrogen elements), which include Li, K, Na, Rb, Fr, and Cs, along with the elements of the lithium group and the S-block [29]. These element's main characteristics are shiny, soft metals with a high level of reactivity. These substances are utilized in HEAs systems in inert gas (Ara and N) environments during mechanical alloying and metal sintering.

3.2. Alkaline earth metals

Alkaline earth metals have group 2 elements: Be, Ca, Mg, Sr, Ra, and Ba [30]. This group of elements primarily consists of low-density metals intended to produce light-weight HEAs.

3.3. Transition metals

The elements present in groups 3 to 12 (other than Ac) are called transition metals. The elements are Sc, Ti, V, Cr, Mn, Fe, Co, Ni, Cu, Zr, Nb, Mo, Tc, Ru, Rh, Pd, Ag, Cd, Hf, Ta, W, Re, Os, Ir, Pt, Au and Hs. This group also has Mt, Ds, Rg, and Cn, but these elements have unknown properties. This group of elements in the D block has strong thermal and electrical conductivity. Most transition metals have oxidation resistance, which prevents corrosion of nearby metal components.

3.4. Post-transition metals

Al, Ga, In, Ti, Zn, Cd, Hg, Sn, Pb, and Bi are post-transition metals that vigorously attack the other adjacent metals. They are soft by nature and have electron junctions.

3.5. Metalloids and non-metals

This element group exhibits metal and non-metal behaviors, which include B, Si, Ge, As, Sb, and Te [31]. In HEAs, generally, metalloids are utilized to increase the FCC crystal structure strength and ductility [32]. Metalloids have favorable structural applications and the biomedical sector [33]. Nonmetals include C, N, O, P, S, and Se. Adding carbon to the Fe alloying system enhances the hardness and decreases the toughness. Neutral nitrogen and oxygen gas reduce the chemical reaction during the heat treatment.

3.6. Halogens

Halogens are mainly salt-producing non-metals with strong reactivity that can be combined to make hydrogen, including F, Cl, Br, I, and At [30]. Group 17 should be utilized to structure it. Due to their greater electronegativity (EN), these elements can produce more electrons than those with strong ionic bonds. Fluorine has a high EV compared to all other ingredients, and Cesium has a comparatively low EV. The sequence of EN is $F > Cl > Br > I > At$.

3.7. Noble gas

Noble gas is also called inert gas. These inert gases help to maintain the minimum amount of reaction or neutral position of alloys during various heat treatments or other processes. It includes He, Ne, Ar, Kr, Xe, Rn, and Og [34].

3.8. Lanthanide

Pr, Ce, Nd, Pm, Sm, Eu, Gd, Tb, Dy, Ho, Er, Tm, Yb, La, and Lu are non-reactive elements. There are F-block elements. Elements are 4F electrons in nature with more binding force. Their hardness and strength are increased due to this binding force. The main application of La serious is to enhance the heat deformation behavior of AZ110 alloy systems [35].

3.9. Actinoids

Th, Pa, U, Np, Pu, Am, Cm, Bk, Cf, Es, Fm, Md, No, Ac, and Lr are categorized as actinoids. Each element of an actinoid is radioactive [36]. An overview of the previously presented data shows that using W, Mo, Ti, and Cr in the alloying system will strengthen the solid solution and enhance the performance of the individual elements. The variables connected to precipitation are Al, Nb, Ti, and Ta. Support for the carbide formers comes from W, Nb, Cr, Ta, Ti, Mo, and V. They improve the material's ability to withstand wear, abrasion, and hardness. The surface stabilizers are Cr, Al, B, and Zr. Mn, Mo, Cr, and Ni are necessary and beneficial for increasing hardness.

4. Forms of HEAs based on different fabrication methods and dimensional effect

Fig. 1 shows the processing of HEAs based on their parent forms like powder, fibers, films, and bulk form. Among them, powder form mechanical alloying is most preferable in zero dimension. Due to its powder nature, homogeneous mixing is ensured. Preparation of HEAs fibers in melt spinning is also a possible technique. HEAs films are primarily used in various coating processes to get a better output in terms of surface properties.

A high-rate vacuum coating method called magnetron sputtering enables the deposition of a wide range of materials, including metals and ceramics. Compared with other approaches, it enables a more rapid deposition rate at less pressure and produces extremely sticky coatings [38]. The limitation of magnetron sputtering is that the thickness of the film is restricted [39]. In laser cladding, a film thickness of up to 50 μm to 2 mm can be achieved. The form of bulk HEAs in arc melting is preferable because of its highly homogenous nature, which enhances mechanical performance.

5. Phase formation rules

HEAs phase prediction and its effect are based on the following aspects.

5.1. Thermodynamic parameters

The kinetic actions are not considered in phase formation. Thermodynamic parameters like Gibbs free energy are the most considered factors in HEAs.

$$\Delta G_{mix} = \Delta H_{mix} - T\Delta S_{mix} \tag{1}$$

The temperature differential, mixing entropy, and mixing enthalpy have all been related to equation (1). This equation addresses the rise in enthalpy and the fall in entropy of mixing. HEAs stability is as follows: configurational entropy, atomic size differences, enthalpy and entropy of mixing, valence electron concentration, and electron per unit cell [40].

5.2. Configurational entropy

Configurational entropy is a significant term for phase selection in HEAs. It is expressed as [41,42].

$$\Delta s_{conf} = -\mathrm{k}\ln\omega = -R\left(\frac{1}{n}\ln\frac{1}{n}+\frac{1}{n}\ln\frac{1}{n}+..\frac{1}{n}\ln\frac{1}{n}\right) = -R\ln\frac{1}{n} \tag{2}$$

$$\Delta s_{mix} = -R\sum_{i=1}^{n} c_i \ln c_i = R\ln n \tag{3}$$

where,

K = Boltzmann constant

ω = Number of ways of mixing.

R = Universal gas constant.

c_i = Mole fraction of i^{th} element

N = Total number of components.

In HEAs, if the value Δs_{conf} is more than 1.10R, the fusion of the elements will happen [42].

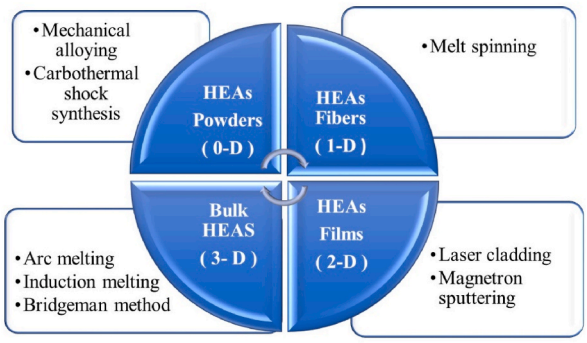

Fig. 1. Overview of the HEAs processing methods [37].

5.3. Atomic size difference (δ) or radius mismatch

The differences in atomic sizes of the alloying systems alter the performance of the strengthening behavior. As well as decreasing the nuclear size difference, it will enhance the single-phase solid solution. In some cases, an increase in atomic size will form an amorphous structure [41]. It reduces the atomic size differently. It should include a better solid solution phase and considerable mixing enthalpy. HEAs generally develop single-phase, reliable solutions [23]. From the Hume rotary rule, atomic size differences should be less than 15% for binary alloys [40]. The atomic size difference was computed by Ref. [41].

$$\delta\,\% = 100\% \times \sqrt{\sum_{i=1}^{n} c_i \left(1 - \frac{r_i}{\sum_{j=1}^{n} c_j r_j}\right)^2} \tag{4}$$

where,

N = Number of various elements.

c_j = Elemental composition of $i^{th}j^{th}$ elements or atomic fraction

r_i, r_j = Atomic radius of $i^{th}j^{th}$ elements

5.4. Enthalpy of mixing in the multi-component alloy

$$\Delta H_{mix} = \sum_{i=1, i\neq 1}^{n} 4\Delta H_{AB}^{mix} c_i c_j \tag{5}$$

where,

ΔH_{AB}^{mix} = Binary alloys mixed entropy

ΔH_{AB}^{mix} It is positive to form compounds and harmful to begin precipitation hardening. More negative to create BMGs - HEAs

5.5. Entropy of mixing in multicomponent alloys

$$\Delta S_{mix} = -R\sum_{i=1}^{N} c_i \ln c_i \tag{6}$$

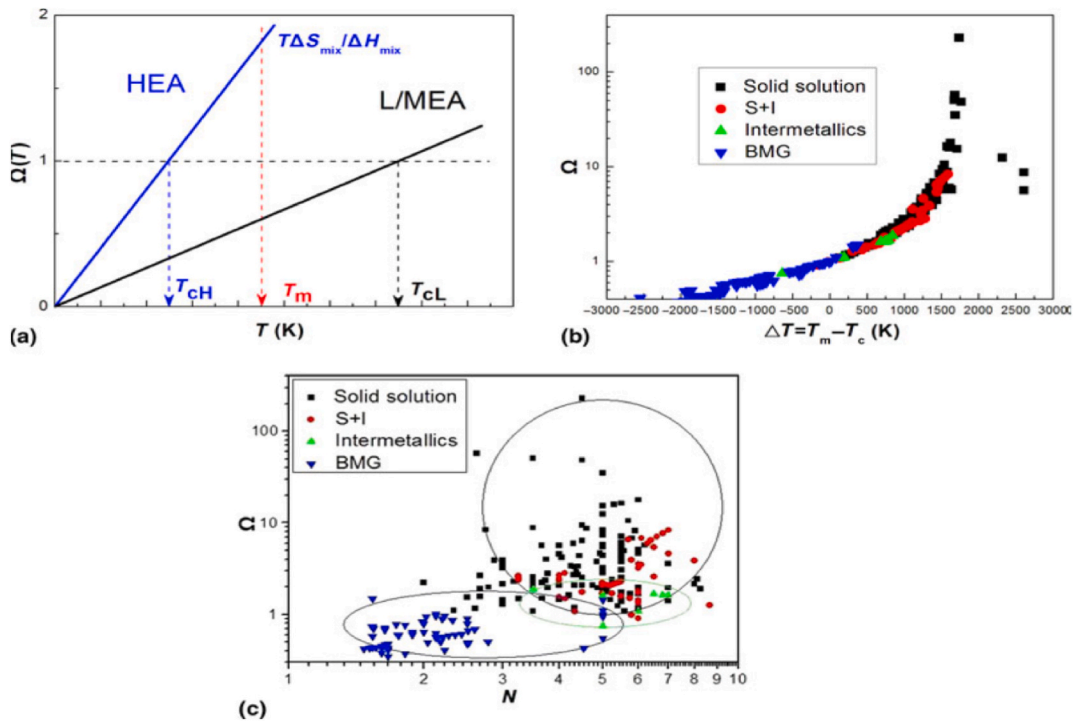

Fig. 2. a. Relationship between various temperatures and combining effect. Fig. 2b. Temperature differences and combining effect. Fig. 2c. Alloying addition (N) to combining effect for the formation of solid solution [42].

As the name implies, high entropy is when the entropy levels are increased in the particular alloy system to reduce element segregation. Then, with decreases in entropy, more element segregation happened. This entropy ranges depend on atomic size different from 12 to 17.5 $J/(mol.k)$ with a significant value of atomic size difference. If the atomic size increases, different entropy ranges from 11 to 16.5 $J/(mol.k)$ [2].

5.6. Combining effect (Ω)

These combining effects are based on average melting temperature, mixed entropy, and enthalpy.

$$\Omega = \frac{T_m \Delta S_{mix}}{|\Delta H_{mix}|} \tag{7}$$

where,

T_m = Average melting temperature = $\sum_{i=1}^{n} c_i\,(T_m)_i$.

$(T_m)_i$ = Melting point of *the* i^{th} component

Equation (7) shows the phase prediction of HEAs. Adding five elements is most favorable for enhancing the combining effect in solid solution phases. Fig. 2a. Illustrates a lower addition of elements to form a bimetallic glass formation at a lower combining effect.

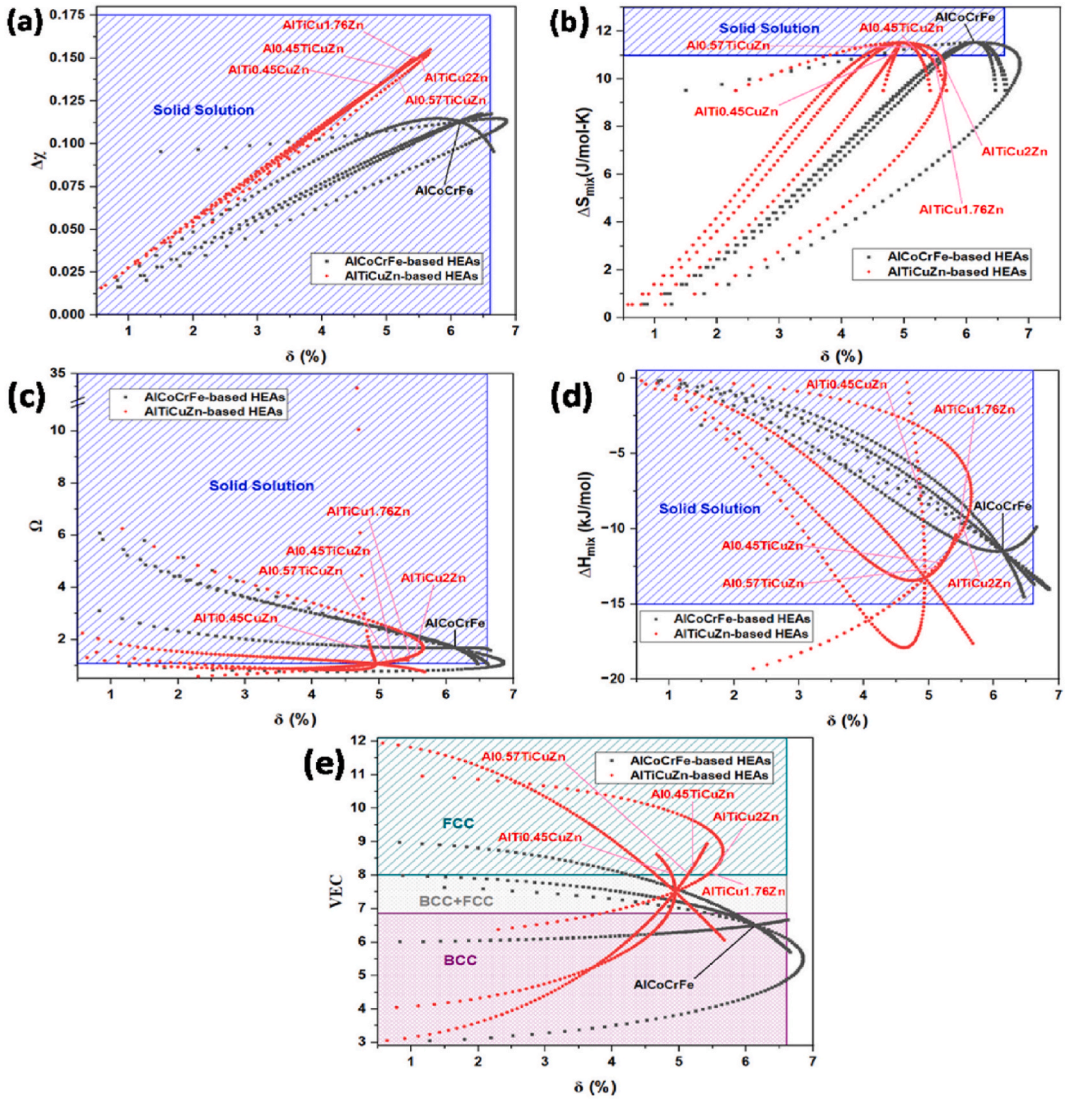

Fig. 3. a. Relation between atomic size different (δ) in % Vs electronegativity. 3b. δ (%) Vs ΔS_{mix}. 3c. δ (%) Vs Ω. 3d δ (%) Vs ΔH_{mix}. 3(e) δ (%) Vs VEC. Comparative study phase formation and its possible outcomes of Al–Co–Cr–Fe and Al–Ti–Cu–Zn based HEAs [45]. Reuse with Journal Permission. Copyrights 2023, Elsevier.

This value Ω ≥ 1.1 and ≤6.6 % of these ranges should form solid solution phases. Larger and smaller represent intermetallic and BMGs. HEAs require several elements to achieve a higher Ω. It may form a major solid solution phase and some solid solution + intermetallic to make it visible. Fig. 2b. Shows high melting point materials with high positive results for the formation of improved solid solution stability and improved combing effect. Fig. 2c. The same as BMGs have to add a lower number of features higher Ω [40].

5.7. Critical solution temperature (T_C)

$$T_{C=\frac{|\Delta H_{mix}|}{\Delta S_{mix}}} \tag{8}$$

The critical solution temperature appears lower than the melting point temperature and Ω. In these conditions, as the melting point temperature is above the critical solution temperature, the solution temperature can be held after solidification. It should be the reverse conditions critical solution temperature attained first, then held on for cooling purposes, followed by a chemical reaction in the liquid phase [43].

5.8. Valence electron concentration (VEC)

Several valence electrons have to be closely occupied in a unit cell. The VEC is mainly used for phase prediction for BCC, FCC, HCP, and sometimes intermetallic compounds. Also, phase stability determines VEC to form the same material at room temperature ductility. FCC phases found at VEC >8.0, BCC phases at VEC< 6.87, and a combination of BCC and FCC stages or intermetallic at 6.87 ≤ VEC <8 [40]. The average VEC of a multicomponent alloy system has been predicted by Ref. [44].

$$VEC_{\ avg} = \sum_{i=1}^{n} c_i\ (VEC)_i \tag{9}$$

Where,

$(VEC)_i$ = Valance electron concentration of i^{th} elements

Summary of the phase formation.

From equations (1)–(9), high negative mixing enthalpy favors the formation of more configurational entropy. Also, adding more alloying elements to the HEAs system generates more entropy. Atomic size differences contribute more to single-state solid solution formation. Differences between atomic radii are less and more favoring BCC structure formation. Different more favor for FCC, BCC + FCC structure higher atomic size different more favor for hydrogen storage application. As a name represents combining effect, it is related to melting temperature, mixed entropy, and enthalpy. Fig. 3a. Based on atomic size differences, changes related to electro-negativity. Fig. 3b. Shows atomic size differences to the effect of ΔS_{mix}, and Fig. 3c. Shows atomic size differences to the effect of Ω. Fig. 3d. Shows atomic size differences to the effect of ΔH_{mix}, and Fig. 3e Shows atomic size differences to the effect of VEC. From Fig. 3 the overall outcome is a higher combined effect with the help of lowering the atomic size difference for solid solution formation. Al–Ti–Cu–Zn-based HEAs are more favorable for the construction of FCC crystal structure, and the addition of Cu is more likely to form a BCC + FCC structure like Al–Ti–$Cu_{1.76}$Zn and high negative mixing enthalpy compared to Al–Co–Cr–Fe. Followed by Al–Co–Cr–Fe favorable for the formation of BCC structure. Temperature effect is a more influential parameter for improved interatomic bonding nature. High melting points (T_m) of elements are more bonding behavior because a high melting point lowers the diffusion rate. i.e., T_m (Cr) > T_m (Fe) > T_m (Co) > T_m (Al) and diffusion rate D for D(Al) > D(Co) > D(Fe) > D(Cr) [45].

6. Physical metallurgy (PM)

Physical metallurgy is one of the subspecialties of material science engineering. The synthesis of different elements is emphasized first; then, their crystal shapes, chemical compositions, microstructures, and mechanical and physical properties are examined [46]. A wide range of core effects follows all the HEAs: high-entropy effect, severe lattice distortion effect, sluggish diffusion effect, and cocktail effect. Determining the benefits and drawbacks of alloy behavior is also made easier with the help of this influence.

6.1. High-entropy effect

HEAs prominent and notable impact is the high entropy effect. It will depend on the impact of thermodynamics. The high entropy of Gibb's free energy impact is then noted. ΔG = ΔH – TΔS. The main variables determining entropy levels are based on Gibb's free energy, system enthalpy, temperature, and entropy [47]. The stability of the HEAs depends on their entropy levels. Then, minimizing or reducing Gibbs free energy enhances alloy stability. Entropy at high temperatures and low free energy are also included [48]. This phenomenon also supports the inter-element solubility of the various alloying elements. However, it is false that at high temperatures, a simple solid solution can form [49].

6.2. Severe lattice distortion effect (SLD- effect)

This effect is based on HEAs in deformation in nature. Additionally, this effect is an interaction between solid-state physics, different strengthening methods, toughness, wear, and creep mechanisms. Atoms should be attracted or repelled from each other

depending on the nature of the electrons in the alloy systems, followed by the SLD effect. Then, different metals and non-metals are combined with varying particle sizes, atomic size differences, crystal structures, strain rates, and metal bonding behavior to generate various alloy systems. These should change both the crystal structure and the impact of the substantial lattice deformation. The BCC structure has more pronounced distortion effects than the FCC. This lattice distortion was estimated using the atomic sizes of numerous distinct elements. The impact of SLD electrical and thermal conductivity is raised due to dispersed electrons and phonons [40]. When compared to conventional alloys, HEAs can detect a higher distortion rate.

6.3. Sluggish diffusion effect

This effect is based on a kinetic nature, and forces are assumed to be involved. In contrast to ordinary alloys, the phase transformation in HEAs manifests a slower diffusion rate than it stabilizes the HEAs system. If the atom's energy level changes during diffusion, it causes vacancy defects. This leads to a mismatch between them; as a result, the particles are restricted and cannot escape, forcing them to migrate to locations with lower energy. When traveling at high energy, atoms have a higher chance of returning to their original location. It functions based on activation energy. Diffusion is additionally slowed down with the help of Co, Cr, Mn, Fe, and Ni [40]. Enhancing the creep resistance while lowering the diffusion rate is necessary [48]. The effect of the lower diffusion rate on grain size should be increased during heat treatment. Increasing grain size with grain boundaries decreases this type of grain, also called coarse grains. However, with HEAs, there is no satisfaction for a slower diffusion rate to increase configurational entropy [49].

6.4. Cocktail-effect

Ranganathan (2003) was the first one to present the cocktail effect using alloy design and its characteristics [50]. This effect alters material magnetization, flexibility, strength, coercivity, and electrical strength. The primary purpose of using this effect is to compromise between strength, plasticity, and coercivity. Coercivity in the electrical field is essential for higher load carrying and long-term operation without damage to the instrument with the help of low coercivity. When coupled efficiently, this effect increases magnetism and decreases coercivity. This effect is mainly used for electrical applications like inductors, transformers, and electrical machines. To evaluate the grain size, dislocation density, and secondary phase formation determined with the assistance of plasticity and coercivity. Reduced coercivity has the effect of improving mechanical properties. Soft magnetic performance within the limits of $\leq$200 A/m is better performance for the limit of coercivity in the HEAs range of 500 A/m. The addition of TiC to the $Fe_{24}Ni_{24}$-$Co_{24}Mn_{18}$-based HEAs system achieved a coercivity of 100.5 A/m and yield strength of 1167 MPa, followed by the ultimate tensile strength of 1212 MPa and 5% elongation [50]. The HEAs system of $Fe_{26}Co_{25}Ni_{20}Cu_{15}Al_{13.1}Ga_{0.9}$ reported a coercivity of 334 A/m and a yield strength of 414.6 MPa [51].

7. Various types of HEAs

7.1. Light-weight HEAs

Lower emission control is the basis for today's material selection criteria. Using the light-weight high-entropy alloy (LW-HEAs) system is essential for many applications. Globally speaking, adopting light-weight materials prevents ozone layer depletion, makes fuel consumption simple, and minimizes CO_2 emissions. Because of this, most HEA families use LW-HEAs. Li, Mg, Al, Si, and Ca are the most widely used low-density elements for choosing lightweight components for alloying addition [52]. Density values $\leq 5\ g/\ cm^3$ are called LW- HEAs [5]. The researcher must describe and modify the density values to account for the various study points of view. Study based on light-weight, low melting-point HEAs near the Mg–Al–Zn–Cu–Mn system to achieve a density of 3.4. Impact or cyclic stress does not use low melting point materials [53]. Iron-based $Fe_{40}Mn_{19}Ni_{15}Al_{15}Si_{10}C_{01}$ density achieved 6.49 g/cm^3 [54]. Additionally, reported density values for the $Al_{20}Li_{20}Mg_{10}Sc_{20}Ti_{30}$ alloy system are 2.67 g/cm^3, and the grain size is 2.67 nm [55]. Construction of $Cr_{24}Mn_{06}Fe_{40}Co_{24}Ni_{06}$ as that system to attain density values of 7.95 g/cm^3 and produce a new class of light-weight metastable HEAs [56]. The addition of Mn in the alloy systems decreased the density from 7.8 to 7.39 g/cm^3 in the alloy system of Al and Si [57]. Alloy system of $Mg_{43}(Mn–Al–Zn–Cu)_{57}$ to achieve a density of 2.51 g/cm^3, $Al_{35}Mg_{30}Si_{13}Zn_{10}Y_7Ca_5$ density of 2.73 g/cm^3. $Al_{20}Li_{20}Mg_{10}Sc_{20}Ti_{30}$ alloy system to achieve a density of 2.67 g/cm^3. The other researcher has to advise the density of 7 $g/\ cm^3$ of alloys including light-weight HEAs [52].

7.2. Nanoprecipitate HEAs

The mechanical alloying process is more beneficial for creating nanomaterials most economically, depending on milling parameters, including milling time, ball-to-powder ratio, and process control agents that influence the formation of nanoparticles. To help create nanosized particles, the ratio of powder to various process control agents was raised. With the help of nanoparticles, it alters the crystal structure and improves its mechanical properties. BCC crystal structure is discussed in most research as being formed by nanosized particles. In HEAs, nanostructured particles prevent undesirable secondary-phase intermetallic particle formations [17]. Moreover, the FCC crystal structure and grain boundary precipitates were undesirable. Because it reduces the ductility and forms an intergranular fracture [58]. The precipitation hardening of copper-based Cu–Ni–Si alloy systems is assessed in continuous and discontinuous precipitation studies based on misorientation angle, grain size, and grain boundary types. Discontinuous precipitates are

more likely to occur at misorientation angles of 30°-50°. Lower misorientation angles promote discontinuous precipitation, and the discontinuous precipitation's interface bonding between the matrix and reinforcement is lower, so for that reason, continuous-type precipitation is preferable and stable. Limitations are reduced the strength [59]. Nanoprecipitation creates particles with a build-a-heat treatment process, and nanoparticles have a size range of 1–100 nm. These phases enable the dendric and inter-dendric phases while reducing the nanostructured particle porosity level [10]. Power transfer units in electric cars and large bandgap semiconductors are utilized for nanoparticles in soft magnetic materials. These capabilities include high saturation magnetization, strong electric resistance, and low coercivity [9].

7.3. Ultrafine-grained HEAs

Compared to other types of HEAs, ultrafine-grained HEAs possess high strength and ductility. Metal hot rolling is the most used process for creating ultrafine-grained HEAs. The achievement of a homogeneous distribution is another goal of hot rolling. A heterogeneous structure offers more robust strength-ductility engagement than a homogeneous structure [60]. The dynamic re-crystalline method enhances ultrafine-grained phases. With the help of dynamic re-crystalline, the strain rate and compressive stress decrease as the metal deformation and temperature increase. This impacts the ultrafine-grained HEAs, and the grain size decreases with the help of mechanical alloying, causing misorientation angles as additional grain boundaries emerge. Grain boundaries with misorientation angles less than $< 10^{\circ}$ are called low-angle ones. Medium-angle grain boundaries occur with an angle between 10° to 15°. Moreover, higher-angle grain boundaries occur greater than 15° [61]. However, most research indicates low-angle grain boundaries have low interfacial energies and higher geometrically necessary dislocation (GND). Higher GND means more intergranular corrosion occurs, and they are immune to precipitation. High-angle grain boundaries were found to show a higher continuity of precipitation [62]. Compared to low-angle grain boundaries, precipitation formed in high-angle grain borders three times as quickly [58]. The microstructure of several ultrafine-grained HEAs produced at high recrystallization temperatures exhibited outstanding resistance to HEAs coarsening [63]. To enable partial recrystallization, the grain size was refined, increasing the strength of HEAs [64].

7.4. Dual phase HEAs (DP-HEAs)

BCC, FCC, HCP, or single-state solid solutions follow most alloy systems. Each alloying system has a unique set of needs. BCC structures, for instance, have a high yield but low ductility. FCC, on the other hand, has a low yield and is highly ductile. The limitations of that single-phase alloy system are the strength-ductility trade-off [65]. The alloy system's choice of BCC or FCC depends on the valency electron concentration. When the VEC is between 6.87 and 8, there is the possibility that a dual-phase structure will form. However, due to its higher field uses, such as turbine blades, contemporary studies have focused on a combined state or dual phase (BCC + FCC). As mentioned, the XRD pattern may show BCC and FCC behavior, with the FCC phase having a higher peak intensity than the BCC phase. Increased peak intensity must make it difficult to determine the crystal structure. Depending on the exact requirements, many alloying systems are available, and some elements are fortified by the crystal structure, such as the BCC structure, which is more affluent with Al and Cr. Fe, Ni, Co, and other elements have been added to the FCC structure. Intriguing results about FCC and HCP in area fraction evaluation on that alloy system investigating $Fe_{50}Mn_{30}Co_{10}Cr_{10}$ (at. %) DP- HEAs. 68% of the grain boundaries in the HCP phase are smaller than 1 μm in length, accounting for 13% of the total area. The FCC phase occupied 78% of all grain boundaries, was <1 μm long, and accounted for 30% of the total area [66]. For dual-phase HEAs Ni–Al, systems are rich in the b_2 phase. The b_2 phase increases the Al content and enhances the hardness, and the b_2 phase achieves more yield strength [67]. Furthermore, Fe–Nb is abundant in the lave phase. The effect of the laves phase is more thermally stable than other phases [68].

7.5. TRIP/TWIN HEAs

The mechanisms of transformation-induced plasticity (TRIP) and twinning-induced plasticity (TWIN) are more effective in balancing strength and ductility in an alloying system over time [69]. To achieve greater strength in alloying systems, various strengthening mechanisms such as precipitate strengthening, interstitial strengthening, and solid solution strengthening. There has been current research on TWIN and TRIP, microband-induced plasticity (MBIP), and stacking fault-induced plasticity (SFIP) have been investigated [70,71]. The stacking fault energy (SFE) of alloy systems is < 20 to stimulate the TRIP effect, and the SFE ranges from 20 to 40 to stimulate the TWIN effect [72]. High SFE is for improved phase stability, and low SFE is for TRIP [1]. SFE typically applies to steel, manganese, copper, and titanium alloys. Ti alloys must attain a higher strain rate [73]. Manganese elements most strongly assist the TWIN/TRIP effect due to a more excellent mix of strength and ductility in addition to 5–12 wt% of Mn. That is called 3-generation Mn development [71]. In this $Fe_{37}Mn_{45}Co_{09}Cr_{09}$ alloy system, TRIP - Dual-phase (DP) HEAs provide much greater strength and ductility than single phase [74].

8. Effects of mechanical alloying in HEAs

8.1. Functions of process control agents in mechanical alloying

Increased product life or durability is a result of mechanical alloying or powder crushing, which aims to improve mechanical performance. Injecting additives increases their effectiveness in the mechanical alloying process. These additives are called process control agents (PCAs). PCAs are surface-active substances, sometimes known as surface additives. PCAs can be either liquid or solid.

Liquid PCAs include toluene, 1,4-dioxane, aniline, isopropyl alcohol, ethyl acetate, pyridine, acetone, ethanol, methanol, N-dimethyl formamide, cyclohexane (C_6H_{12}) water [75]. And hexane and polyethylene glycol [76]. A solid PCA is a stearic acid. The primary role of PCAs is to maintain equal stability levels between the powder particles during cold welding and act as surface agents. Milling time is an essential factor in changing the crystallinity of the alloying system. Changes in crystallinity are more favorable for increasing/decreasing the strength and stiffness and altering the corrosion resistance properties. Negative effects of change in the % of ductility. To increase the milling time from 0 to 60 h, crystallinity changes are minimized with an increase in the milling time in PCAs addition. Without the addition of PCAs, more changes in the crystallinity after 30 h. Results with the addition of PCAs % of crystallinity changes minimized for a prolonged time if mechanical alloying [77]. Fig. 4. Shows the effect of crystallinity changes with and without the addition of PCAs.

The evaluation of mechanical attributes impacts the crystalline structure. The amounts of carbon and oxygen present altered the crystalline structure of the alloying system. PCAs for stearic acid, methanol, and n-heptane are in dry and wet conditions. Out of all these PCAs, methanol contains the highest percentage of oxygen. Furthermore, n-heptane and stearic acid have the most carbon [75]. Fig. 5a, b, 5c. Shows the amount of carbon and oxygen levels of methanol, stearic acid, and n-heptane of various PCAs.

However, adding ethanol to the ball milling process increases the power recovery rate by 4%. The impact of ethanol is to improve structural and magnetic characteristics [78]. Methanol burns quickly, is flammable, and is volatile—a comparison of methanol and toluene shows. Additionally, there is less pollution, consisting of 11% toluene and 4% methanol. After milling, the nature of toluene provides a higher proportion of carbon, 1.3%, in mechanical alloying (MA) samples. In comparison to dry milling at 0.2% and methanol at 0.8%, this effect was lessened [28]. Stearic acid does not fail to alloy quickly and, like PCAs, depreciates at a substantially slower temperature. Initially composed of $Ni_{50}Ti_{25}Al_{25}$, the alloy percentage combination was changed by adding PCAs after milling to $Ni_{52.66}Ti_{25.74}Al_{21.60}$ influence of PCAs. This finding indicates that PCAs proof alters their chemical properties and phase structure [79]. The effect of increasing the amount of stearic acid in the Fe and Ni system is that the elemental particle size reduces, and then the fraction increases, so Fe and Ni are not suitable for stearic acid [80]. Commonly used additions that contribute to MA are 1–5 wt%. In PCAs, the active components prevented agglomeration; they absorbed the particle surface, lowering surface tension. When compared to the $Al_XCoCrFeMnNi$ alloy system. The chemical characteristics of PCAs, such as stearic acid, lowest vapor pressure and highest boiling point, methanol highest vapor pressure and lowest boiling point, and n-heptane influence particle size and volume percentage changes. At that time of MA, adding PCAs to the Al and Cr had a stronger attraction for oxygen, while Fe, Cr, and Mn had a stronger affinity for carbon [76]. Moreover, PCAs reduce the surface contact of powder particles when using oil or organic solvents [47]. Additionally, the PCAs cyclohexane and Phosphonobutane tricarboxylic acid (PBTC) were used. Other phases, such as carbide and oxide, are present above the powder range of 60 nm. Compared to stearic acid, methanol, PBTC, and cyclohexane, cyclohexane is capable of influencing the nanostructure through mechanical alloying, and one appealing outcome is that it reduces carbon and oxygen production [81]. For 60 h of milling, increase the weight percentage (1, 2, 3, 4) of stearic acid to cause the morphology to shift from a spherical to a plate-like structure [82]. Fig. 6. Shows a change in morphology with an increase in the % of PCAs. Fig. 6 a, b. Shows without stearic acid PCAs. Fig. 6c. For 1 wt% of stearic acid, Fig. 6d. For 2 wt % of stearic acid, Fig. 6e. For 3 wt% of stearic acid, Fig. 6f. For 4 wt% of stearic acid [82].

8.2. Mechanical alloying (MA) and its effects

Using the mechanical alloying (MA) technique, the most popular way to reduce particle size and fine-tune grain size is achieved [83]. Which can achieve chemical homogeneity in composition [84]. MA, also known as high-energy ball milling, is created during mechanical alloying by mechanochemical reactions involving solid-solid and solid-liquid interactions. Based on two different types of

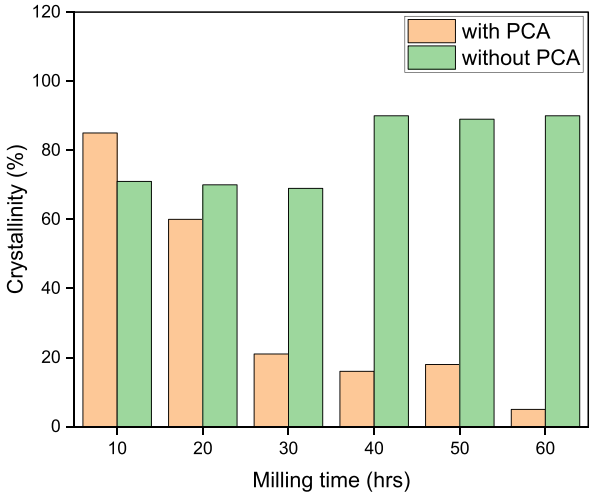

Fig. 4. Milling time-dependent crystallinity changes with and without PCAs effect [77]. Reuse with journal permission. Copyrights 2023, Elsevier.

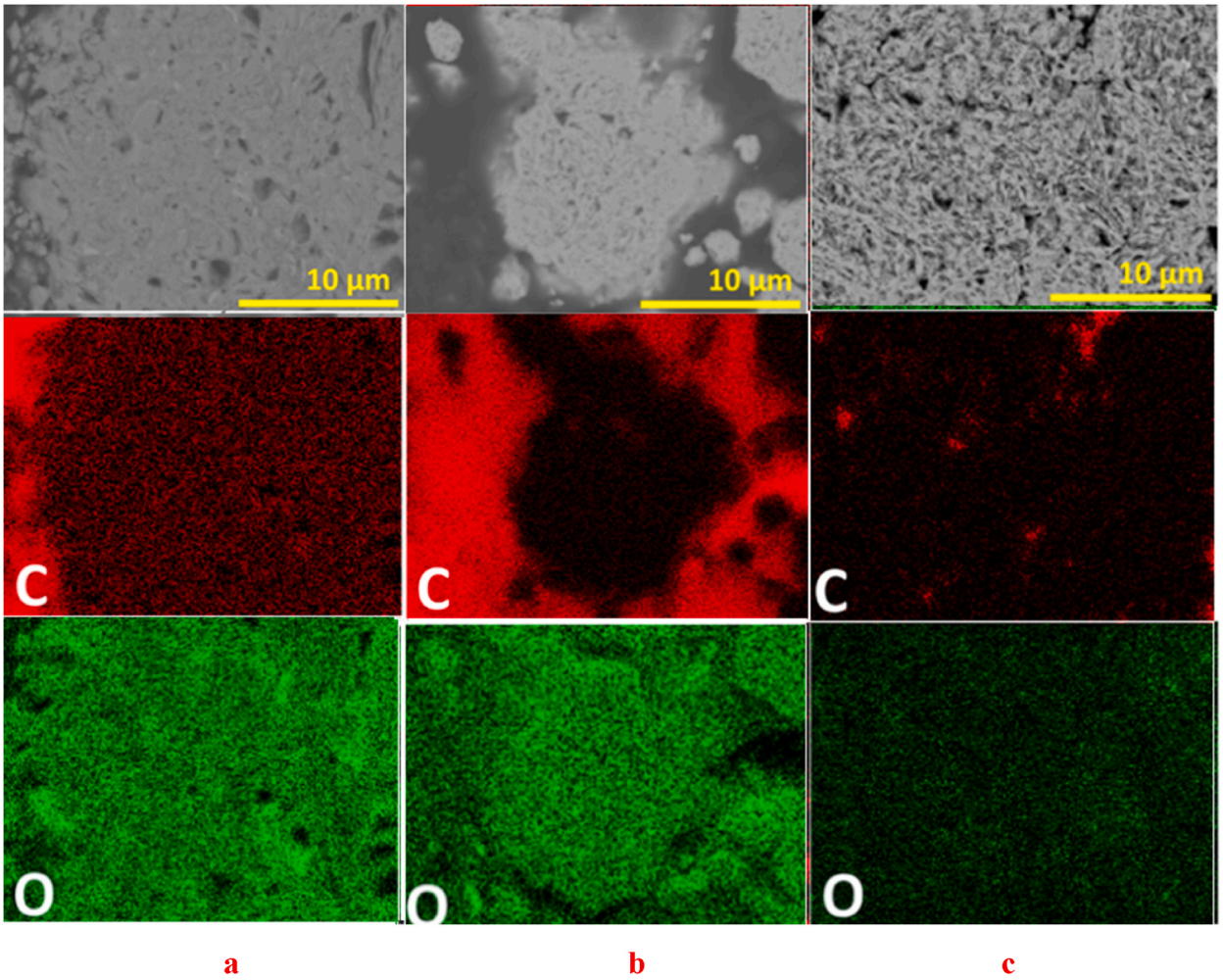

Fig. 5. Effects of carbon and oxygen presents over the various PCAs. Fig. 5a. For methanol. Fig. 5b. For stearic acid. Fig. 5c. For n-heptane [75]. Reuse with journal permission. Copyrights 2023, Elsevier.

responses in milling circumstances, the self-propagating combustion reaction promotes high enthalpy during milling. Another incremental reaction happens gradually. When they collide, their reactions spread within a tiny volume [84]. The ball-to-powder ratio, powder volume, vial volume, milling speed, milling time, ball material, ball diameter, number of balls employed, process control agents, and break interval time are some variables that affect the MA [85]. Composites of Ti–6Al–4V alloy with graphene and As reinforcement, TiBw were added, and Alcohol was included in the PCAs. To get a good dispersion of the combined powder, it will work on MA. With this alloying method, alloys based on aluminium saw an increase in tensile strength from 1098 MPa to 1182 MPa after 8 h of ball milling. However, elongation decreased to 15.1% from 16.0%. Poor ductility as well as plasticity for long hours of milling. Additionally, it encourages the alloy system's cracking [86]. Regarding mechanical properties, the Al alloy created by MA demonstrated a rise in yield strength from 74 MPa to 308 MPa. and a rise in compressive strength from 203 MPa to 526 MPa. Lower the strain rate to 46.52% from 90.62% [87]. Two techniques are used by powder metallurgy to decrease the powder particles' size. High-energy ball milling (HEBM) and stirred milling are two examples. When compared to high-energy ball milling, stirred milling is 40% more energy-efficient. In 13 min, with equal amounts of milling time, HEBM consumes 54.27 kWh/t, and stirred milling consumes 32.45 kWh/t [88]. Milling times should be evaluated based on phase formation, microstructure, hardness, compressive strength, and magnetic properties. The phase change occurs in the BCC-to-FCC structure in the FeCoNiMnAl alloy system after up to 30 h of milling. Magnetic properties decrease as compressive strength increases [89]. During MA, the polydispersity index (PDI) impact concentrates on particle size dispersion throughout various sizes or dimensions. It exhibits the uniformity of the particle size distribution. A PDI of 0.7 denotes a uniform dispersion over a restricted range. All samples have PDI values of less than 0.7, which guarantees that the particle size distribution is consistent within a narrow range [90]. Ball milling impacts powder particle size compared to other techniques, such as MA and arc melting. It reveals that HEAs made using MA have 15% better improvements than those made using arc melting. Several peaks in the XRD study vanished as the MA duration increased maximum density for a faster milling process [17].

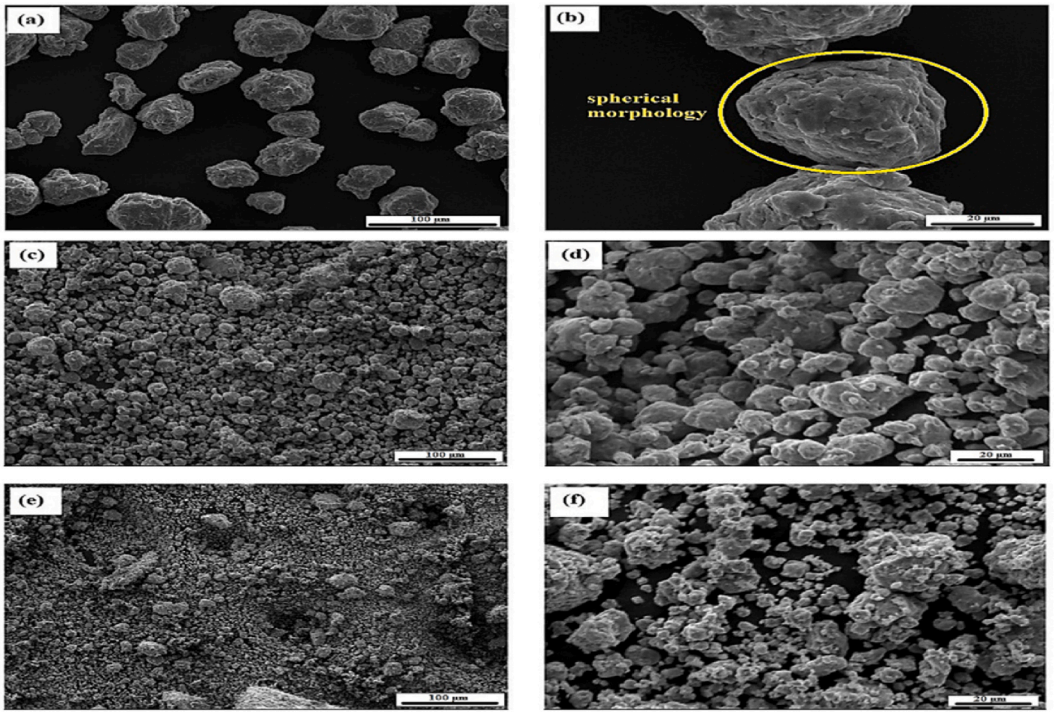

Fig. 6. a, b without stearic acid PCAs. Fig. 6c. 1 wt% of stearic acid. Fig. 6d. 2 wt % of stearic acid. Fig. 6e. 3 wt% of stearic acid. Fig. 6f. 4 wt% of stearic acid [82].

8.3. Metal compactions

Metal compaction is one of the processes in powder metallurgy that comes after mechanical alloying but before metal sintering. Metal compaction aims to achieve uniform densification, produce a fine-grain homogenous microstructure, and lessen metal powder

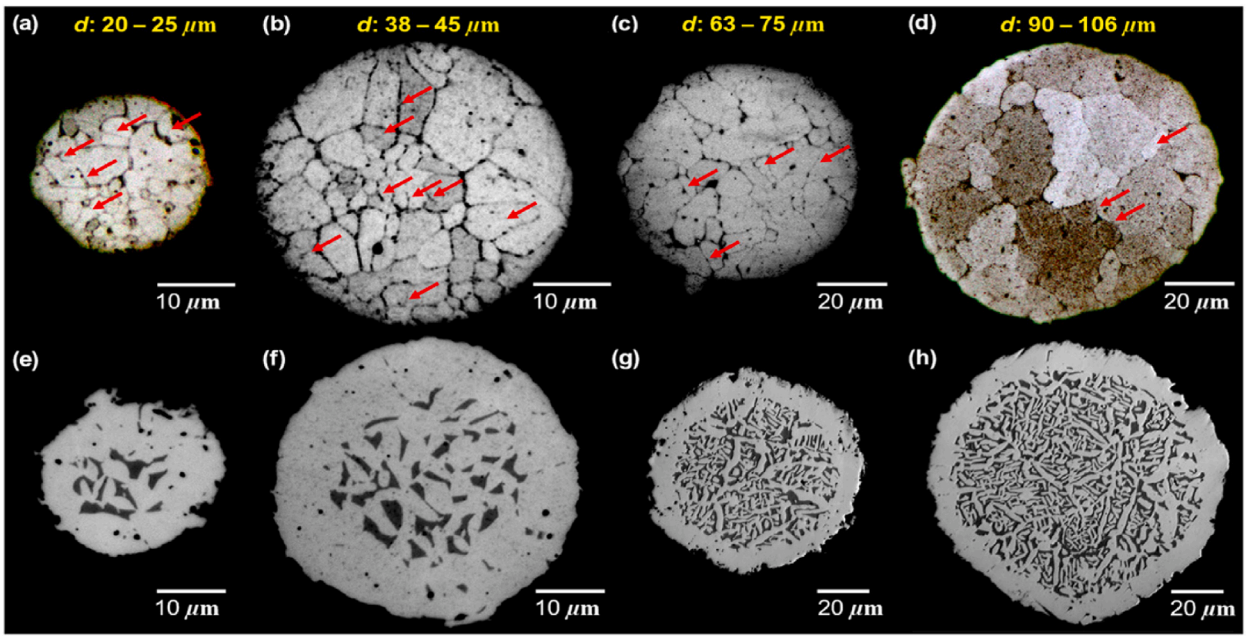

Fig. 7. Influence of temperature condition as-quenched. Fig. 7 a, b, c, d for quenched condition and Fig. 7. e, f, g, h for annealed condition with different grain sizes [96]. Reuse with Journal Permission. Copyrights 2023, Elsevier.

particle segregation. Two kinds of compaction processes are utilized in powder metallurgy: cold and hot compaction. Hot isostatic compaction enhanced the metallurgical bonding, uniform grain structure, and powder particle packing density. Hot compaction has a variety of drawbacks, including higher equipment costs, longer production times, fewer production parts, a wider dimensional tolerance, and the emergence of abrasive surface-active coatings. At 20 °*C*, cold isostatic compactions are effective. Higher and lower pressure levels, superior surface finishes, and more extensive production volumes contribute to better working conditions. The restriction results in less efficient stress relief [91]. Unlike multiaxial compression dies, uniaxial compression die compaction produces more precise results. Additionally, increased compaction pressure leads to decreased metal porosity [16]. The metal particle size of 60 μm reduces interparticle porosity, whereas lowering the porosity levels will depend on how much the particle size is reduced [92].

8.4. Metal sintering

During metal sintering, temperature fluctuations will directly reflect modifications in the mechanical properties and microstructure. High-temperature materials usually have good wear resistance but fail more frequently because of their thermal stability. Powder metallurgy uses several methods, including suction casting, microwave sintering, spark plasma sintering (SPS), tubular furnace sintering, hot isostatic pressing (HIP) under higher pressure, and metal injection molding (MIM), to produce HEAs [13]. The density of the sintered sample decreases as the sintering temperature increases. Minimal concentrations of alloying metals like nickel enhanced the sintering performance of HEAs systems [87]. Reducing porosity and improving density are essential for improving mechanical performance. This way, SPS conditions must be changed for a bulk sample to avoid porosity [93]. Compared to SPS, microwave sintering is significantly more porous [94]. High-frequency induction heating and traditional sintering are being contrasted (HFIHS + CS). Compared to CS 80% densification alone, HFIHS + CS has achieved a higher level of densification to reach 95%. The carbide stage is part of the HEAs sintering process. BCC-cuboidal precipitates were created by conventional sintering at 1200 °*C*, and BCC plate-like precipitates were produced by repeating the procedure with CS + HFIHS at 600 °*C* [18]. Compared to SPS sintering, microwave sintering has the advantages of excellent product purity and quick reaction ignition due to the application of heat by magnetrons [95]. Fig. 7. Shows as-quenched and annealed condition samples in optical micrographs image with grain size. The effect of particle size distribution has a function of dislocation density and microstructure followed by phase transformation. Reduction of particle size linearly increased the dislocation density (BCC structure), and due to their larger surface area to volume ratio, smaller particles cause more localized stresses and strains when being processed and increase the grain boundary (GB) length at a time the higher number of grains inside the GB there is one of the reasons for dislocation motion appeared. Hard precipitates located in GB are one of the reasons for the reduction in GB dislocations. Fig. 7. Shows influence of temperature condition. Fig. 7 a, b, c, and d for quenched samples and Fig. 7 e, f, g, and h for annealed samples. For that, different diameters of the grains grain sizes 20–25 μm decrease the dislocation for others. A number of twin boundaries are one of the reasons for reducing the dislocation density [96].

9. Microstructural effects of HEAs

Any alloy system can easily be identified by its microstructure, which reveals the modifications made to the source components. To discover crack formation, undesired phase evaluation, and oxidation behavior are determined with the help of microstructure. A microstructure analysis utilizing a scanning electron microscope (SEM), electron back-scattered diffraction (EBSD), and transmission electron microscope (TEM) was used. To analyse how five or more elements in an alloy system behave differently. HEAs mechanical properties are better than those of Ni- and Co-based superalloys, and they also have high microstructure stability compared to superalloy systems [50]. HEAs of the Al–Cr–Fe–Ni–V system underwent annealing heat treatment at temperatures of 573 K, 873 K, 1173 K, and 1473 K. L_{12} phases identified in the 1173 K and 1473 K temperature limits. Introducing L_{12} phases improves HEAs high hardness and provides excellent corrosion resistance. An increase in annealing temperature from 1173 K to 1473 K caused an increase in volume fraction and nanoprecipitation along the grain boundary, which led to a harder-to-achieve hardness [22]. AlFeCuNiMgZn HEAs have produced powder metallurgy routes, and their properties were assessed using a scanning electron microscope (SEM). The outcome was followed by an extension of the milling duration after 30 h. The metal porosity will be decreased by creating a dual-phase microstructure and extending the milling procedure [95]. High entropy alloy made of Cr–Mn–Fe–Co–Mo using powder metallurgy by ball milling followed by pressure-less sintering by microstructure effects of four phases present: two BCC, σ (sigma), and μ (mu). At 800 °*C*, as formed by precipitation, a considerably Cr rich σ phase is present. Mo stabilizes the σ phase in Fe-based HEAs. In comparison between the σ (sigma) and μ. σ phase enhances the solid solution in high-temperature applications [97]. AlCoCrCuFeNi HEAs alloy's yield strength was 1750 MPa in the as-cast state below 645 °*C* in 5 h, and the plastic strain rate was under 7.5%. The alloy's microstructure did not change at this temperature. However, the alloy microstructure changed above 645 °*C*, and the FCC phase was reached. As the temperature rises, the alloy system likewise shows a decrease in strength and an increase in plastic strain [98]. For all alloying systems, the influence of dendritic microstructure is more beneficial in lowering the electrochemical corrosion rate when 5 at. % of Mn becomes present [99].

10. Mechanical properties of HEAs

10.1. Hardness

The processing routes significantly influence the hardness of HEAs. HEAs range in hardness from 140 HV to 900 HV. The FCC phase hardness is lower at room temperature than the BCC structure [2]. The alloy system of Al_x-Co-Cr-Cu-Fe-Ni from the study material's

hardness evaluation under various conditions, including as-annealed, as-rolled, and as-homogenized, yielded higher hardness in as-rolled at 399 ± 11 HV than in as-annealed at 250 ± 3 HV, and in as-homogenized at 154 ± 4 HV. Comparing the rolled sample to the annealed sample using fractography revealed that the rolled selection at 600 °*C* created dimples ranging from 2 to 5 μm. At an increase in temperature of 800 °*C*, the dimples are 10 μm. In annealed samples up to 600 °*C* and 800 °*C*, respectively, grain-boundary sliding and intergranular rupture enhanced at this temperature [100]. Fig. 8 (a) shows the hardness levels between as-cast and annealed conditions [39]. Compared to cast conditions, annealed conditions have better hardness. 8 (b) Shows the hardness level of HEAs compared to conventional alloys [101].

A1 = Cu–Ti–V–Fe–Ni–Zr, A2 = Al–V–Ti–Fe–Ni–Zr,

A3 = Ti–Cu–V–Fe–Ni–Zr–Co, A4 = Al–V–Ti–Fe–Ni–Zr–Co–Cr, A5 = 6Al–Ti–4V.

HEAs produce the BCC phase structure with the help of valence electron concentration and improved hardness. A single-phase solid solution generates high hardness while uniformly spreading the alloy ingredient [5]. The author discovered increasing the amount of X (values in 1, 1.5, 2, 2.5, and 3 M ratios) in the specific alloy system to raise the hardness to obtain 740 HV in the Alx-Co-Cr-Fe-Ni alloy system. The lattice constant increased from 2.878 nm to 2.887 nm as the x value increased. However, do not also add the lattice strain [102]. Fig. 8b shows that adding elements Ni, Mn, Mo, and Nb is most favorable for enhancing the hardness up to 700 to 900 HV.

10.2. Nanoindentation

One of the unique characteristics of material characterization procedures for hard alloys and soft materials is the nanoindentation test. Typically, tests, including material hardness, Young's modulus, shear strain distribution, and materials to determine dislocation behavior, are performed and evaluated using the nanoindentation test. The parameters are estimated using the loading force and indentation depth. Molecular dynamics (MD) simulations help to determine the precipitation. The precipitations are barriers to the dislocation motion in the Fe–Co–Ni–Cr–Cu HEAs system. Due to copper's lower deformation rate than other elements, its precipitations are excellent for reinforcing the aluminium alloy system [103]. The hardness of a material is influenced by temperature. Due to the alloy system AlxCoCrFeNi, the hardness of the material decreases as temperature rises, as seen by the increase in indentation depth to the worm surface [104]. Because copper has a high solubility limit in the CoCrNiCu alloy system, it will have an impact on the microstructure in two areas: 1) Dendrites and 2) Inter-dendritic zones, regions Compared to the dendritic phase, the inter-dendritic phase is harder. That means copper content in the dendrite's region changes during heat treatment [105]. Presently, Al is used in both industrial and home settings. Al 6061 combined with RF of graphene and multi-walled CNTs with or without copper coating. High hardness and high strength were attained in Al-6061 with coated MWCNTs + graphene compared to uncoated CNTs + graphene [106].

10.3. Wear

Metallic materials, including Al, Fe, Mg, Ti, and V, have less wear-resistant behavior than HEAs. However, recent studies have concentrated on high wear resistance by adding multiple alloying elements. HEAs have two times the wear resistance of conventional standard alloy systems. In HEAs, there are as many distinct self-characteristics as there are high hardness levels. High-hardness materials have high wear resistance [107]. Four types of wear are considered in engineering applications, like adhesive wear [108]. Abrasive wear [109]. Corrosive wear [110]. Surface-fatigue wear/delamination wear [111]. Al and Ti are added to the Alx--$Co_{1.5}$Cr–Fe–$Ni_{1.5}$Ti HEAs to produce adhesive wear behavior. Al-rich regions form precipitation with a needle-like structure. The

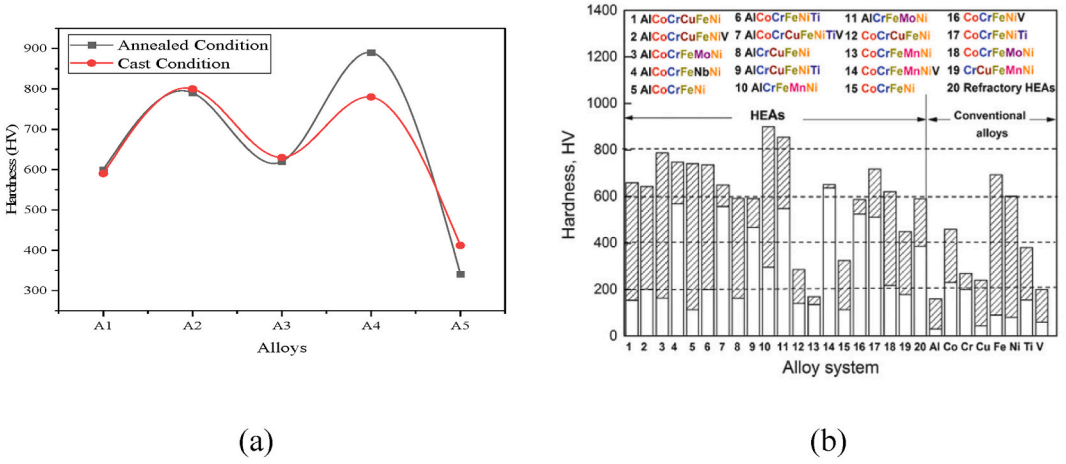

Fig. 8. (a) Comparison of the same compositions of alloys through various heat treatment conditions. (b) Comparison between hardness level between conventional Vs. HEAs [101].

Table 3
Fabrication of HEAs through various methods and its result.

HEAs	RF	FM	PCAs	Hardness	TS	Elongation (%)	CS1	YS	UTS	ΔH mix	ΔS mix	VEC	Ω	δ	Refs
CoCrFeNiMn	Graphene	VHPS	Tert-butanol	298.5 to 377.6	834.04	26.08	2069.66	–	–	–	–	–	–	–	[117]
AlLiMgBeTiCu	–	–	–	326	–	24	–	863	1375	−21.0	11.52	6.75	–	–	[118]
AlCrFeNi	TiO2(4 wt %)	FAST	–	679	–	–	–	–	–	–	–	–	–	–	[119]
CrCuFeNiAl	–	LR	Ethanol	–	–	–	–	–	–	−1.74	12.99	8.1	10.4	4.36	[120]
CrMnFeCoMo	–	P.L. Sintering	Toluene	9.3 ± 0.3 GPa	–	–	–	–	–	−0.77	13.38	7.2	–	4.18	[121]
FeCoNiAlSi	–	SPS	Stearic acid	524–798 HV	–	–	1325–2031 Mpa	–	–	–	–	–	–	6.2	[122]
FeMnCoCr	–	BM	–	–	–	25.5–28.1	–	490	1107	–	–	–	–	–	[123]
CrMnFeCoNi	–	VHPS	N-heptane	–	–	4 to 5	–	115 MPa	1300 ± 11.6 MPa	–	–	–	–	–	[124]
MgTiVZrNb	–	BM	–	–	–	–	–	–	–	7.67	12.59	4.3	–	7.31	[125]
AlCrFeMnNiW	–	BM	–	–	–	–	–	–	–	−2.64	14.89	5.312	11.1	7.94	[126]
MgZrTiFeCoNi	–	HEBM	–	–	–	–	–	–	–	−13.8	14.43	5.22	–	15.61	[127]
TiZrMnFeCr	–	BM	–	–	–	–	–	–	–	−10.7	12.92	5.8	–	9.71	[128]
TiZrFeMnCrV	–	BM	–	–	–	–	–	–	–	−13.4	13.38	5.8	–	9.9	[129]

material's hardness and wear resistance will increase as Ti forms new solubility limits [112]. Al–Ni alloy generates the disordered BCC structure, although when compared to the disordered BCC, the ordered BCC structure has the highest hardness [113]. Wear resistance increased with the help of HEAs prepared with ceramic oxide coatings (hard anodizing coating, cemented carbide coating). Various oxide layer coatings in HEAs, including Al_2O_3, Fe_2O_3, Cr_2O_3, NiO, and TiO_2, are favored. An increased concentration of Ti in an alloy system increases the hardness of the material because Ti has a more negative enthalpy. The negative enthalpy provides better stability for reinforced materials. Due to this reason, Ti is harder [4]. Wear resistance in HEAs is also improved by various strengthening mechanisms like dispersion and solution strengthening [114]. Effect of wear performance upon addition of various reinforcements (RF), including Cu–B_4C (flake morphology), Cu-fly ash (spherical morphology), and Cu–W (fine spherical shape), among the three reinforcements. Cu–B_4C is more appropriate for wear applications, while Cu–W works better in electrical applications [115]. Increasing the amount of Al in a Cu–Al alloy system causes Cu to change to Cu_2O and Al to change to Al_2O_3, which increases wear resistance. The oxide layer has the best wear resistance [116]. Table 3 shows the fabrication of HEAs through various fabrication methods and its results. Fig. 9. Explains the behavior of materials under strain hardening and yield stress condition.

11. HEAs – applications

The HEAs will aid in producing furnace components and aircraft engine parts since they can sustain high-temperature phase stability and have outstanding oxidation resistance for high-temperature applications. Used for jigs and fixtures in industry, fuel cells, solar cells, hydrogen storage devices, and supercapacitors are energy storage and transmission equipment. Automotive applications include brake drums, brake pads, and energy-transfer devices such as clutches. Used for underwater plumbing for oil pumping and transportation equipment. Fig. 10 shows the HEAs field application based on alloy selection.

12. Summary

This review paper focused on forming the HEAs, various factors and parameters to be considered, phase formation rules, and the physical metallurgy techniques found in published literature. The effects of mechanical alloying in HEAs, microstructural effects, and mechanical properties of HEAs are also presented. Various types of HEAs like light weight HEAs, nanoprecipitate HEAs, dual-phase HEAs, ultrafine-grained HEAs, and TRIP/TWIN HEAs and their application areas are presented.

13. Future scope

Modern materials have significantly benefited from the discovery of alloys, and in this direction, the HEAs are crucial. The world needs to do more to conserve energy. Light-weight materials like Li, Mg, Be, Al, and Ti are primarily chosen for reducing CO_2 emissions, battling global warming, lowering fuel costs, and facilitating transportation. Another instance is low-density elements (less than 5). The crystal structures, like BCC and FCC, are opposite. This behavior is due to overcoming the TWIN/TRIP effect on strength-ductility balance. However, this effect has introduced a new product called invisible MEAs (IMEAs). The IMEAs design system improves strength-ductility more than MEAs and HEAs [130]. And the future research on materials will be in this direction.

Data availability statement

This manuscript is a review paper and doesn't have any numerical or experimental data to disclose.

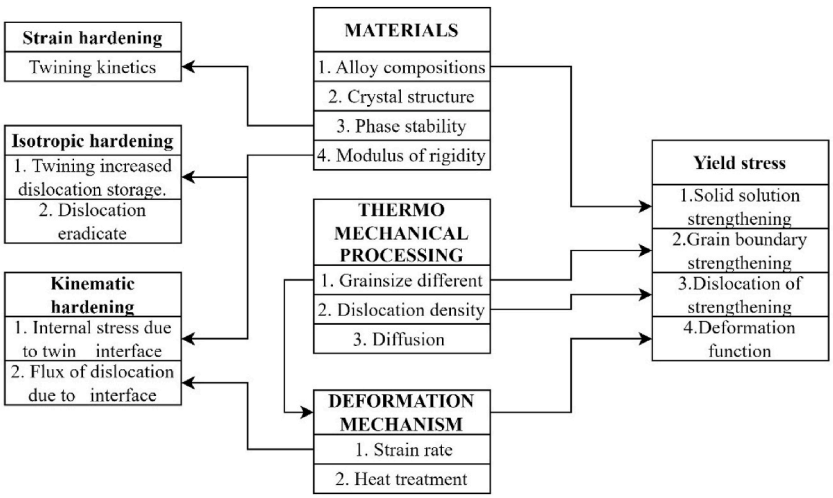

Fig. 9. Flow diagrams of alloy performance in strain hardening and yield stress based on materials.

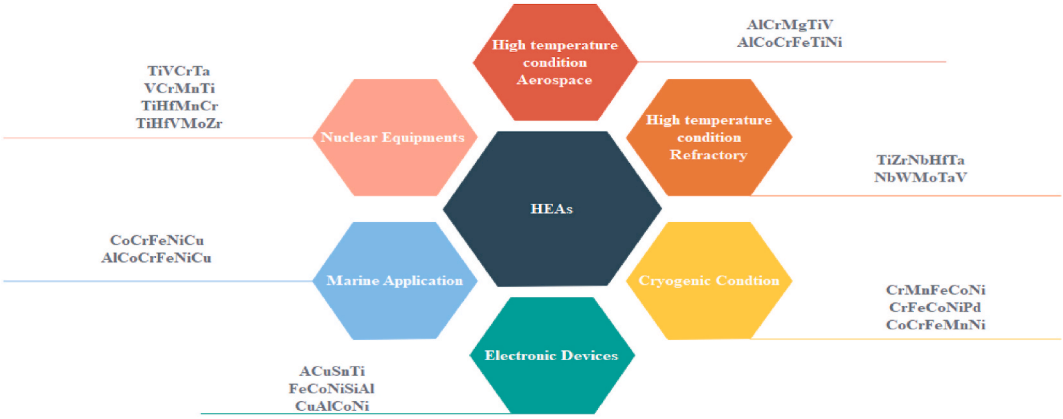

Fig. 10. Applications of HEAs in various fields [130].

CRediT authorship contribution statement

Balaji V: Compilation, Drafting, Editing and Final Document Prepraration. **Anthony Xavior M:** Writing – review & editing, Supervision.

Declaration of competing interest

The authors declare that they have no known competing financial interests or personal relationships that could have appeared to influence the work reported in this paper.

Nomenclature section

AN - Atomic Number
ASTM - American Society for Testing and Materials
BCC - Body Cantered Cubic
BMGs Bulk Metallic Glasses
CCAs - Compositional Complex Alloys
CS - Conventional Sintering
CS_1 - Compressive Strength
DP-HEAs - Dual Phase High Entropy Alloys
E — Element
EBSD - Electron Back-Scattered Diffraction
EN_1 - Element Name
EN - Electronegativity
FCC - Face Cantered Cubic
FM - Fabrication Methods
GND - Geometrically Necessary Dislocation
HCP - Hexagonal Close-Packed
HEAs - High Entropy Alloys
HEBM - High Energy Ball Milling
HFIHS - High-Frequency Induction Heat Sintering
HIP - Hot Isostatic Pressing
HV - Vickers Hardness Number
VEC - Valence Electron Concentration
IMEAs - Immiscible Medium Entropy Alloys
LC - Laser Cladding
LWHEAs - Light Weight High Entropy Alloys
MA - Mechanical Alloying
MBIP - Microband-Induced Plasticity
MCAs - Multiprinciple Component Alloys (MCAs)
MD - Molecular Dynamics
MEAs - Medium Entropy Alloys
MIM - Metal Injection Molding

MWCNTs - Multi-Walled Carbon nanotubes
PBTC - Phosphonobutane Tricarboxylic Acid
PCAs - Process Control Agents
PDI - Polydispersity Index
PM - Physical Metallurgy
RF - Reinforcements
SFE - Stacking Fault Energy
SFIP - Stacking Fault-Induced Plasticity
SEM - Scanning Electron Microscope
SLD - Severe Lattice Distortion
SPS - Spark Plasma Sintering
T_C - Critical solution temperature
TEM - Transmission Electron Microscope
T_M - Melting Points
TRIP - Transformation Induced Plasticity
TS - Tensile Strength
TWIN - Twinning Induced Plasticity
UTS - Ultimate Tensile Strength
XRD - X-Ray Diffraction
Y Modulus - Young's Modulus

References

[1] X. Wu, D. Mayweg, D. Ponge, Z. Li, Microstructure and deformation behavior of two TWIP/TRIP high entropy alloys upon grain refinement, Mater. Sci. Eng. 802 (2020) 140661, https://doi.org/10.1016/j.msea.2020.140661.
[2] Y. Zhang, C.C. Koch, S.G. Ma, H. Zhang, Y. Pan, High Entropy Alloys Fundamentals and Applications.China, Springer, Cham, 2016, https://doi.org/10.1007/978-3-319-27013-5_5.
[3] H. Zhang, S. Lei, Y. Li, S. Cui, S. Hu, P. Wang, Microstructural evolution and magnetic and corrosion properties of $FeCoNiA_{l0.2}Y_x$ High-Entropy Alloys, ECS J. Solid State Sci. Technol. 12 (2023) 113009, https://doi.org/10.1149/2162-8777/ad0876.
[4] C. Junyu, Y. Yu, P. Yuzheng, Y. Yang, H. Liwen, H. Meilong, Wear resistance performance of high entropy alloy-ceramic coating composites synthesized via a novel combined process, Chin. J. Chem. Eng. 57 (2023) 202–213, https://doi.org/10.1016/j.cjche.2022.08.010.
[5] H. Heydari, M. Tajally, A. Habibolahzadeh, Calculations to introduce some light high entropy alloys based on phase formation rules, J. Alloys Compd. 912 (2022) 165222, https://doi.org/10.1016/j.jallcom.2022.165222.
[6] B. Hu, G. Shen, Z. Wang, S. Li, Y. Wang, H. Luo, Ultrahigh tensile strength achieved in a light-weight medium Mn steel via prominent work hardening, J. Mater. Sci. Technol. 145 (2023) 156–164, https://doi.org/10.1016/j.jmst.2022.11.009.
[7] M. Gupta, K.S. Tun, An insight into the development of light weight high entropy alloys, Res. Develop. Material Sci. 6 (9) (2016) 199, https://doi.org/10.31031/RDMS.2017.02.000534.
[8] M.I. Khan, F. Shah, T. Hayat, A. Alsaedi, Transportation of CNTs based nanomaterial flow confined between two coaxially rotating disks with entropy generation, Phys. Stat. Mech. Appl. 527 (2019) 121154, https://doi.org/10.1016/j.physa.2019.121154.
[9] Y. Ye, et al., Exceptional soft magnetic properties of an ordered multi - principal element alloy with disordered nanoprecipitates, High Entropy Alloys Materials 1 (2023) 165–174, https://doi.org/10.1007/S44210-022-00010-8.
[10] H. Kalantari, M. Zandrahimi, M. Adeli, H. Ebrahimifar, The production of nanocrystalline AlCoCrFeNiTiZn high entropy alloy via mechanical alloying : study of the formation mechanism , microstructural evolution , and magnetic properties of the alloy, Intermetallics 150 (2022) 107694, https://doi.org/10.1016/j.intermet.2022.107694.
[11] M. Sadeghi, B. Niroumand, Design and characterization of a novel MgAlZnCuMn low melting point light weight high entropy alloy (LMLW-HEA), Intermetallics 151 (2022) 107658, https://doi.org/10.1016/j.intermet.2022.107658.
[12] S. M. K, P. Rukmini, S. Charan, P.C. V Mohan, ScienceDirect effect of high entropy alloy crystallite size on structural behavior and hardness of Al-MMC, Mater. Today Proc. 24 (2020) 724–730, https://doi.org/10.1016/j.matpr.2020.04.328.
[13] N.B. Pradeep, M.M.R. Hegde, S. Rajendrachari, A.O. Surendranathan, Investigation of microstructure and mechanical properties of microwave consolidated TiMgSr alloy prepared by high energy ball milling, Powder Technol. 408 (2022) 117715, https://doi.org/10.1016/j.powtec.2022.117715.
[14] N.F. Shkodich, et al., Refractory TaTiNb, TaTiNbZr, and $TaTiNbZr_X$ (X = Mo, W) high entropy alloys by combined use of high energy ball milling and spark plasma sintering_ Structural characterization, mechanical properties, electrical resistivity, and thermal conductivity, J. Alloys Compd. 893 (2022) 162030, https://doi.org/10.1016/j.jallcom.2021.162030.
[15] C. Liu, X. Jiang, H. Sun, Y. Zhang, Y. Fang, Microstructure and mechanical properties of bioinspired laminated CoCrFeNiMn high entropy alloy matrix composites reinforced with graphene, Mater. Sci. Eng. 859 (2022) 144198, https://doi.org/10.1016/j.msea.2022.144198.
[16] Y. Kim, D. Lee, J. Hwang, H. Jin, S. Hyung, Fabrication and characterization of powder metallurgy tantalum components prepared by high compaction pressure technique, Mater. Char. 114 (2016) 225–233, https://doi.org/10.1016/j.matchar.2016.03.005.
[17] A. Crfenico, H.R. Ammar, S. Sivasankaran, A.S. Alaboodi, F.A. Al-mufadi, Synthesis, Microstructural investigation and compaction behavior of $Al_{0.3}CrFeNiCo_{0.3}Si_{0.4}$ nanocrystalline high entropy alloy, Adv. Powder Technol. 32 (2021) 398–412, https://doi.org/10.1016/j.apt.2020.12.016.
[18] S. González, Evaluation of high-frequency induction heat sintering and conventional sintering in $Al_xCoCrFeMnNi$ high-entropy alloys, J. Alloys Compd. 910 (2022) 164780, https://doi.org/10.1016/j.jallcom.2022.164780.
[19] E. Wu, et al., The rendering from the periodic system of elements on the stability, elastic, and electronic properties of M_2AX phases, Materialia 27 (2023) 101676, https://doi.org/10.1016/j.mtla.2023.101676.
[20] C.-J. Tong, et al., Microstructure characterization of $Al_xCoCrCuFeNi$ high-entropy alloy system with multiprincipal elements, Metall. Mater. Trans. 36 (2005) 881–893, https://doi.org/10.1007/s11661-005-0283-0.
[21] B. Kang, J. Lee, H.J. Ryu, S.H. Hong, Ultra-high strength WNbMoTaV high-entropy alloys with fine grain structure fabricated by powder metallurgical process, Mater. Sci. Eng. 712 (2018) 616–624, https://doi.org/10.1016/j.msea.2017.12.021.
[22] Z. Liu, et al., Heat treatment induced microstructural evolution and strength enhancement of Al–Cr–Fe–Ni–V high-entropy alloy fabricated by laser powder bed fusion, Mater. Sci. Eng. 861 (2022) 144348, https://doi.org/10.1016/j.msea.2022.144348.

[23] M. Calin, et al., Tailoring biocompatible Ti-Zr-Nb-Hf-Si metallic glasses based on high-entropy alloys design approach, Mater. Sci. Eng. C 121 (2021) 111733, https://doi.org/10.1016/j.msec.2020.111733.

[24] Fuyang Tian, et al., Empirical design of single phase high-entropy alloys with high hardness, Intermetallics 58 (2015) 1–6, https://doi.org/10.1016/j.intermet.2014.10.010.

[25] Che-Wei Tsai, et al., Effect of temperature on mechanical properties of Al0.5CoCrCuFeNi wrought alloy, J. Alloys Compd. 490 (2010) 106–165, https://doi.org/10.1016/j.jallcom.2009.10.088.

[26] Mahammad Ali, Golla Shaik, Development of highly wear resistant Cu - Al alloys processed via powdermetallurgy, Tribol. Int. 136 (2019) 127–139, https://doi.org/10.1016/j.triboint.2019.03.055.

[27] M. GUPTA, Multiple component alloys: the way forward in alloy design, Material Sci. Res. India 16 (2019), https://doi.org/10.13005/msri/160101, 01–03.

[28] D.B. Miracle, O.N. Senkov, A critical review of high entropy alloys and related concepts, Acta Mater. 122 (2017) 448–511, https://doi.org/10.1016/j.actamat.2016.08.081.

[29] J.L. Dye, The Alkali Metals : 200 Years of Surprises, vol. 373, Philosophical Transactions Of The Royal Scciety A, 2015, https://doi.org/10.1098/rsta.2014.0174.

[30] John Emsley, Nature's Building Blocks: an A-Z Guide to the Elements, Oxford University Press, Oxford, 2001.

[31] R.E. Vernon, Which elements are metalloids, J. Chem. Educ. 90 (2013) 1703–1707, https://doi.org/10.1021/ed3008457.

[32] D. Wei, et al., Metalloid substitution elevates simultaneously the strength and ductility of face-centered-cubic high-entropy alloys, Acta Mater. 225 (2022) 117571, https://doi.org/10.1016/j.actamat.2021.117571.

[33] B.S. Sekhon, Metalloid compounds as drugs, Res. Pharmaceut. Sci. 8 (3) (2013) 145–158. PMID: 24019824.

[34] Z. Mazej, Noble-gas chemistry more than half a century after the first report of the noble-gas compound, Molecules 25 (13) (2020) 3014, https://doi.org/10.3390/molecules25133014.

[35] Q. Liao, et al., Hot deformation behavior and processing map development of AZ110 alloy with and without addition of La-rich Mish Metal, J. Mater. Sci. Technol. 61 (2021), https://doi.org/10.1016/j.jmst.2020.04.064, 1–15.

[36] S.T. Liddle, International year of the periodic table: lanthanide and actinide chemistry, Angew. Chem. Int. Ed. 58 (16) (2019) 5140–5141, https://doi.org/10.1002/anie.201901578.

[37] Y. Zhang, Q. Xing, High entropy alloys: manufacturing routes. Encyclopedia of materials: metals and alloys, Encyclopedia Materials, Metals Alloys 2 (2022) 327–338, https://doi.org/10.1016/B978-0-12-803581-8.12123-X.

[38] X. Hu, T. Wang, F. Li, X. Mao, Surface modifications of biomaterials in different applied fields, RSC Adv. 13 (30) (2023) 20495–20511, https://doi.org/10.1039/D3RA02248J.

[39] Y. Li, Y. Shi, Phase assemblage and wear resistance of laser-cladding $Al_{0.8}FeCoNiCrCu_{0.5}$ Sixhigh-entropy alloys on aluminum, Mater. Res. Express 7 (8) (2020), https://doi.org/10.1088/2053-1591/aba9f7, 0–9.

[40] Y.F. Ye, Q. Wang, J. Lu, C.T. Liu, Y. Yang, High-entropy alloy: challenges and prospects, Mater. Today 19 (6) (2016) 349–362, https://doi.org/10.1016/j.mattod.2015.11.026.

[41] J.W. Yeh, et al., Nanostructured high-entropy alloys with multiple principal elements: novel alloy design concepts and outcomes, Adv. Eng. Mater. 6 (5) (2004), https://doi.org/10.1002/adem.200300567, 299–303.

[42] Y. Zhang, et al., Guidelines in predicting phase formation of high-entropy alloys, MRS Communicat. 4 (2) (2014) 57–62, https://doi.org/10.1557/mrc.2014.11.

[43] K. Balasubramanian, S.V. Khare, D. Gall, Valence electron concentration as an indicator for mechanical properties in rocksalt structure nitrides, carbides and carbonitrides, Acta Mater. 152 (15) (2018) 175–185, https://doi.org/10.1016/j.actamat.2018.04.033.

[44] J.W. Yeh, Recent progress in high-entropy alloys, Annales de chimie, Science des Materiaux 31 (6) (2006) 633–648, https://doi.org/10.3166/acsm.31.633-648.

[45] Intekhab Alam, A. Moses, Revisiting the phase stability rules in the design of high-entropy alloys: a case study of quaternary alloys produced by mechanical alloying, Intermetallics 159 (2023) 107919, https://doi.org/10.1016/j.intermet.2023.107919.

[46] A. Banerjee, R. Prasad, V.N. Vaidya, Gibbs free energy of formation of the ternary oxide Nd_3RuO_7, J. Alloys Compd. 420 (1–20) (2006) 283–285, https://doi.org/10.1016/j.jallcom.2005.10.038.

[47] M.H. Tsai, J.W. Yeh, High-entropy alloys: a critical review, Materials Res. Letters 2 (3) (2014) 107–123, https://doi.org/10.1080/21663831.2014.912690.

[48] S.K. Dewangan, A. Mangish, S. Kumar, A. Sharma, B. Ahn, V. Kumar, A review on High-Temperature Applicability: a milestone for high entropy alloys, Engineering Science and Technolog, Int. J. J. 35 (2022) 101211, https://doi.org/10.1016/j.jestch.2022.101211.

[49] S. Ranganathan, Alloyed pleasures: multimetallic cocktails, Curr. Sci. 85 (10) (2003) 1404–1406. http://eprints.iisc.ac.in/id/eprint/6189.

[50] T. Chen, W. Chen, R. Wu, C. Chu, Z. Jiang, Z. Fu, Microstructure and properties of $TiC/Fe_{24}Ni_{24}Co_{24}Mn_{18}$ high-entropy composite with exceptionally low coercivity, Mater. Today Commun. 35 (2023) 106150, https://doi.org/10.1016/j.mtcomm.2023.106150.

[51] M. Gupta, An insight into the development of light weight high entropy alloys, Res. Developm. Material Sci. 2 (2) (2017), https://doi.org/10.31031/rdms.2017.02.000534, 123–125.

[52] H. Kalantari, M. Zandrahimi, M. Adeli, H. Ebrahimifar, The production of nanocrystalline AlCoCrFeNiTiZn high entropy alloy via mechanical alloying: study of the formation mechanism, microstructural evolution, and magnetic properties of the alloy, Intermetallics 150 (2022) 107694, https://doi.org/10.1016/j.intermet.2022.107694.

[53] H. Jain, Y. Shadangi, D. Chakravarty, K. Chattopadhyay, A.K. Dubey, N.K. Mukhopadhyay, Low-density $Fe_{40}Mn_{19}Ni_{15}Al_{15}Si_{10}C_1$ high entropy steel processed by mechanical alloying and spark plasma sintering: phase evolution, microstructure and mechanical properties, Mater. Sci. Eng. 869 (2023) 144776, https://doi.org/10.1016/j.msea.2023.144776.

[54] K.M. Youssef, A.J. Zaddach, C. Niu, D.L. Irving, C.C. Koch, A novel low-density, high-hardness, high-entropy alloy with close-packed single-phase nanocrystalline structures, Materials Research Letters 3 (2) (2015) 95–99, https://doi.org/10.1080/21663831.2014.985855.

[55] K.N. Yoon, H.S. Oh, J.Y. Kim, M.S. Kim, J. Zhang, E.S. Park, A new class of light-weight metastable high entropy alloy with high strength and large ductility, Materialia 21 (2022) 101284, https://doi.org/10.1016/j.mtla.2021.101284.

[56] B. Hu, G. Shen, Z. Wang, S. Li, Y. Wang, H. Luo, Ultrahigh tensile strength achieved in a light-weight medium Mn steel via prominent work hardening, J. Mater. Sci. Technol. 145 (2023) 156–164, https://doi.org/10.1016/j.jmst.2022.11.009.

[57] Z. Zhang, N.C. Parson, W.J. Poole, Precipitation on grain boundaries in Al-Mg-Si alloys: the role of grain boundary misorientation, Scripta Mater. 211 (2022) 114494, https://doi.org/10.1016/j.scriptamat.2021.114494.

[58] X. Liao, et al., Effect of misorientation of grain boundaries on the discontinuous precipitates of Cu–Ni–Si alloy, J. Mater. Res. Technol. 26 (2023) 2060–2069, https://doi.org/10.1016/j.jmrt.2023.08.056.

[59] A.X. Li, P.F. Yu, Y.P. Gao, M.T. Dove, G. Li, Ultra-high strength and excellent ductility high entropy alloy induced by nano-lamellar precipitates and ultrafine grain structure, Mater. Sci. Eng. 862 (2022), https://doi.org/10.1016/j.msea.2022.144286, 1–10.

[60] Q. Liu, G. Wang, Y. Liu, X. Sui, Y. Chen, S. Luo, Hot deformation behaviors of an ultrafine-grained MoNbTaTiV refractory high-entropy alloy fabricated by powder metallurgy, Mater. Sci. Eng. 809 (2021) 140922, https://doi.org/10.1016/j.msea.2021.140922.

[61] J. Desai Choundraj, J. Kacher, Influence of misorientation angle and local dislocation density on β-phase distribution in Al 5xxx alloys, Sci. Rep. 12 (2022) 1–8, https://doi.org/10.1038/s41598-022-05948-8.

[62] S.H. Joo, et al., Structure and properties of ultrafine-grained CoCrFeMnNi high-entropy alloys produced by mechanical alloying and spark plasma sintering, J. Alloys Compd. 698 (2017) 591–604, https://doi.org/10.1016/j.jallcom.2016.12.010.

[63] Z. Yang, D. Yan, W. Lu, Z. Li, A TWIP-TRIP quinary high-entropy alloy: tuning phase stability and microstructure for enhanced mechanical properties, Mater. Sci. Eng. 801 (2021) 140441, https://doi.org/10.1016/j.msea.2020.140441.

[64] R.N. Li, H.Y. Song, M.R. An, M.X. Xiao, Atomic-scale insight into mechanical properties and deformation behavior of crystalline/amorphous dual-phase high entropy alloys, Phys. Lett. 446 (2022) 128272, https://doi.org/10.1016/j.physleta.2022.128272.

[65] C. Chen, et al., Microstructure of and mechanical properties of an as-cast fine-grain dual-phase Fe-based high entropy alloy formed via solid-state phase transformation, Mater. Sci. Eng. 838 (2022) 142779, https://doi.org/10.1016/j.msea.2022.142779.

[66] Z. Ye, et al., Realizing superior strength-ductility combination in dual-phase AlFeCoNiV high-entropy alloy through composition and microstructure design, Materials Res. Letters 10 (11) (2022) 736–743, https://doi.org/10.1080/21663831.2022.2093140.

[67] L. Gu, et al., Novel as-cast NiAlCoFeNb dual-phase high-entropy alloys with high hardness, Mater. Lett. 324 (2022) 132676, https://doi.org/10.1016/j.matlet.2022.132676.

[68] L. Ma, J. Wang, P. Jin, Microstructure and mechanical properties variation with Ni content in Microstructure and mechanical properties variation with Ni content, Mater. Res. Express 831 (2020) 154873, https://doi.org/10.1016/j.jallcom.2020.154873.

[69] K. Yuan, Y. Jiang, S. Liu, S. Xu, X. Li, X. Wu, Effect of carbon upon mechanical properties and deformation mechanisms of TWIP and TRIP-assisted high entropy alloys, Mater. Sci. Eng. 857 (2022) 144126, https://doi.org/10.1016/j.msea.2022.144126.

[70] A.K. Patra, C.N. Athreya, S. Mandal, K.C. Hari Kumar, V. Subramanya Sarma, High strength-high ductility medium Mn steel obtained through CALPHAD based alloy design and thermomechanical processing, Mater. Sci. Eng. 810 (2021) 140756, https://doi.org/10.1016/j.msea.2021.140756.

[71] Z.Y. You, et al., Microstructural design and deformation behavior of a TRIP/TWIP tri-phase heterogeneous high-entropy alloy, Intermetallics 156 (2023) 107854, https://doi.org/10.1016/j.intermet.2023.107854.

[72] G.H. Zhao, X. Xu, D. Dye, P.E.J. Rivera-Díaz-del-Castillo, Microstructural evolution and strain-hardening in TWIP Ti alloys, Acta Mater. 183 (2020) 155–164, https://doi.org/10.1016/j.actamat.2019.11.009.

[73] Z. Li, K.G. Pradeep, Y. Deng, D. Raabe, C.C. Tasan, Metastable high-entropy dual-phase alloys overcome the strength-ductility trade-off, Nature 534 (2016) 227–230, https://doi.org/10.1038/nature17981.

[74] P. Mehulkumar Gandhi, S. Kumar Valluri, M. Schoenitz, E. Dreizin, Effect of organic liquid process control agents on properties of ball-milled powders, Adv. Powder Technol. 33 (1) (2022) 103332, https://doi.org/10.1016/j.apt.2021.10.024.

[75] M.A. Ruiz-Esparza-Rodríguez, et al., Influence of process control agent and Al concentration on synthesis and phase stability of a mechanically alloyed Al_xCoCrFeMnNi high-entropy alloy, J. Alloys Compd. 882 (2021) 160770, https://doi.org/10.1016/j.jallcom.2021.160770.

[76] M. Montoya Rangel, J.M. Marín Ramírez, L. Tirado Mejía, M.H. Medina Barreto, B. Cruz Muñoz, Process control agent effect on the structural and magnetic properties of mechanically alloyed Fe(Al) disordered system, J. Magn. Magn Mater. 538 (2021) 168246, https://doi.org/10.1016/j.jmmm.2021.168246.

[77] Mohammad Hossein Khazaei Feizabad, Shahriar Sharafi, et al., Effect of process control agent on the structural and magnetic properties of nano/amorphous $Fe_{0.7}Nb_{0.1}Zr_{0.1}Ti_{0.1}$ powders prepared by high energy ball milling, J. Magn. Magn Mater. 449 (2018) 297–303, https://doi.org/10.1016/j.jmmm.2017.10.018.

[78] J. Shi, A. Zheng, Z. Lin, R. Chen, J. Zheng, Z. Cao, Effect of process control agent on alloying and mechanical behavior of L21 phase Ni–Ti–Al alloys, Mater. Sci. Eng. 740–741 (2019) 130–136, https://doi.org/10.1016/j.msea.2018.10.097.

[79] K. Gheisari, S. Javadpour, The effect of process control agent on the structure and magnetic properties of nanocrystalline mechanically alloyed Fe-45% Ni powders, J. Magn. Magn Mater. 343 (2013) 133–137, https://doi.org/10.1016/j.jmmm.2013.05.007.

[80] R. Juárez, J.J. Suñol, R. Berlanga, J. Bonastre, L. Escoda, The effects of process control agents on mechanical alloying behavior of a Fe-Zr based alloy, J. Alloys Compd. (2007) 434–435, https://doi.org/10.1016/j.jallcom.2006.08.108, 472–476.

[81] G. Popescu, et al., Mechanically alloyed high entropy composite, IOP Conf. Ser. Mater. Sci. Eng. 145 (2007), https://doi.org/10.1088/1757-899X/145/7/072007.

[82] Negar Yazdani, Shabani Ali, Effects of process control agent amount, milling time, and annealing heat treatment on the microstructure of AlCrCuFeNi high-entropy alloy synthesized through mechanical alloying, Metals 11 (2021) 1493, https://doi.org/10.3390/met11091493.

[83] D. Yang, et al., A novel FeCrNiAlTi-based high entropy alloy strengthened by refined grains, J. Alloys Compd. 823 (2020) 153729, https://doi.org/10.1016/j.jallcom.2020.153729.

[84] V. Udhayabanu, N. Singh, B.S. Murty, Mechanical activation of aluminothermic reduction of NiO by high energy ball milling, J. Alloys Compd. 497 (1–2) (2010) 142–146, https://doi.org/10.1016/j.jallcom.2010.03.089.

[85] B.R. Golla, Highly strong aluminum via ball milling and high pressure hot press, Manufacturing Letters 36 (2023) 18–21, https://doi.org/10.1016/j.mfglet.2023.01.001.

[86] H. Wang, H.M. Zhang, X.W. Cheng, S. Chang, X.N. Mu, Effect of ball milling time on microstructure and mechanical properties of graphene nanoplates and TiBw reinforced Ti–6Al–4V alloy composites, Mater. Sci. Eng. 861 (2022) 144240, https://doi.org/10.1016/j.msea.2022.144240.

[87] T. Santosh, C. Eswaraiah, R.K. Soni, S. Kumar, Size reduction performance evaluation of HPGR/ball mill and HPGR/stirred mill for PGE bearing chromite ore, Adv. Powder Technol. 34 (1) (2023) 103907, https://doi.org/10.1016/j.apt.2022.103907.

[88] W. Luo, et al., Effects of milling time on the microstructure and properties of FeCoNiMnAl magnetic high-entropy alloys, Mater. Today Commun. 34 (2023) 104777, https://doi.org/10.1016/j.mtcomm.2022.104777.

[89] H.R. Ammar, S. Sivasankaran, A.S. Alaboodi, F.A. Al-Mufadi, Synthesis, microstructural investigation and compaction behavior of $Al_{0.3}$CrFeNi$Co_{0.3}Si_{0.4}$ nanocrystalline high entropy alloy, Adv. Powder Technol. 32 (2) (2021) 398–412, https://doi.org/10.1016/j.apt.2020.12.016.

[90] A.S. Lemine, O. Fayyaz, R.A. Shakoor, Z. Ahmad, J. Bhadra, N.J. Al-Thani, Effect of cold and hot compactions on corrosion behavior of p- and n-type bismuth telluride-based alloys developed through microwave sintering process, J. Alloys Compd. 939 (2023) 168763, https://doi.org/10.1016/j.jallcom.2023.168763.

[91] B. Sreenu, R. Sarkar, S.S.S. Kumar, S. Chatterjee, G.A. Rao, Microstructure and mechanical behaviour of an advanced powder metallurgy nickel base superalloy processed through hot isostatic pressing route for aerospace applications, Mater. Sci. Eng. 797 (2020) 140254, https://doi.org/10.1016/j.msea.2020.140254.

[92] P. Chauhan, S. Yebaji, V.N. Nadakuduru, T. Shanmugasundaram, Development of a novel light-weight $Al_{35}Cr_{14}Mg_6Ti_{35}V_{10}$ high entropy alloy using mechanical alloying and spark plasma sintering, J. Alloys Compd. 820 (2020) 153367, https://doi.org/10.1016/j.jallcom.2019.153367.

[93] E. Colombini, R. Rosa, L. Trombi, M. Zadra, A. Casagrande, P. Veronesi, High entropy alloys obtained by field assisted powder metallurgy route: SPS and microwave heating, Mater. Chem. Phys. 210 (2018) 78–86, https://doi.org/10.1016/j.matchemphys.2017.06.065.

[94] K. Sai Maneesh, P. Rukmini, S. Charan Reddy, C.V. Mohan Rao, Effect of high entropy alloy crystallite size on structural behavior and hardness of Al-MMC's, Mater. Today Proc. 24 (2020) 724–730, https://doi.org/10.1016/j.matpr.2020.04.328.

[95] P. Pradhan, Y. Shadangi, V. Shivam, N.K. Mukhopadhyay, Powder metallurgical processing of CrMnFeCoMo high entropy alloy: phase evolution, microstructure, thermal stability and mechanical properties, J. Alloys Compd. 935 (2023) 168002, https://doi.org/10.1016/j.jallcom.2022.168002.

[96] Sangho Jeon, et al., Particle size effects on dislocation density, microstructure, and phase transformation for high-entropy alloy powders, Materialia 18 (2021) 101161, https://doi.org/10.1016/j.mtla.2021.101161.

[97] L.H. Wen, H.C. Kou, J.S. Li, H. Chang, X.Y. Xue, L. Zhou, Effect of aging temperature on microstructure and properties of AlCoCrCuFeNi high-entropy alloy, Intermetallics 17 (4) (2009) 266–269, https://doi.org/10.1016/j.intermet.2008.08.012.

[98] S.C. Shi, C.F. Liu, T.T. Fang, T.H. Chen, Effects of Mn addition on mechanical properties, fracture surface, and electrochemical corrosion resistance of CoCrFeNiAl high-entropy alloys, Mater. Res. Express 10 (2023) 074002, https://doi.org/10.1088/2053-1591/ace4a2.

[99] C.W. Tsai, M.H. Tsai, J.W. Yeh, C.C. Yang, Effect of temperature on mechanical properties of $Al_{0.5}$CoCrCuFeNi wrought alloy, J. Alloys Compd. 490 (1–2) (2010) 160–165, https://doi.org/10.1016/j.jallcom.2009.10.088.

[100] C. Li, J.C. Li, M. Zhao, Q. Jiang, Effect of aluminum contents on microstructure and proerties of Al_xCoCrFeNi alloys, J. Alloys Compd. 504 (2010), https://doi.org/10.1016/j.jallcom.2010.03.111. S515–S518.

[101] Diao, et al., Mechanical Properties of High Entropy Alloys, springer, 2016, https://doi.org/10.1007/978-319-27013-5_6.

[102] A. Mu, et al., Nanoindentation into FeCoNiCrCu high-entropy alloy: an atomistic study, Mater. Sci. Technol. 37 (2) (2021) 202–209, https://doi.org/10.1080/02670836.2021.1885095.

[103] Z.M. Jiao, M.Y. Chu, H.J. Yang, Z.H. Wang, J.W. Qiao, Nanoindentation characterised plastic deformation of a $Al_{0.5}$CoCrFeNi high entropy alloy, Mater. Sci. Technol. 31 (10) (2015) 1244–1249, https://doi.org/10.1179/1743284715Y.0000000048.

[104] Y. Ren, et al., A wear-resistant metastable CoCrNiCu high-entropy alloy with modulated surface and subsurface structures, Friction 10 (2022) 1722–1738, https://doi.org/10.1007/s40544-022-0606-9.
[105] V. Kumar, U.N. Kempaiah, Shivasharanayyaswamy, S.B. Bopanna, Nanoindentation studies on multiwalled carbon nanotubes/graphene reinforced aluminium alloy 6061 nanocomposites, Mater. Today Proc. 45 (2021) 202–206, https://doi.org/10.1016/j.matpr.2020.10.418.
[106] X.F. Wang, Y. Zhang, Y. Qiao, G.L. Chen, Novel microstructure and properties of multicomponent CoCrCuFeNiTi$_x$ alloys, Intermetallics 15 (3) (2007) 357–362, https://doi.org/10.1016/j.intermet.2006.08.005.
[107] Y.K. Singla, N. Arora, D.K. Dwivedi, Dry sliding adhesive wear characteristics of Fe-based hardfacing alloys with different CeO_2 additives – a statistical analysis, Tribol. Int. 105 (2017) 229–240, https://doi.org/10.1016/j.triboint.2016.10.015.
[108] G. Xiao, Y. Zhang, B. Zhu, H. Gao, Y. Huang, K. Zhou, Wear behavior of alumina abrasive belt and its effect on surface integrity of titanium alloy during conventional and creep-feed grinding, Wear 514–515 (2023) 204581, https://doi.org/10.1016/j.wear.2022.204581.
[109] M. Wu, R.C. Setiawan, D.Y. Li, Benefits of passive element Ti to the resistance of AlCrFeCoNi high-entropy alloy to corrosion and corrosive wear, Wear (2022) 204231, https://doi.org/10.1016/j.wear.2021.204231, 492–493.
[110] P. Kulu, R. Veinthal, M. Saarna, R. Tarbe, Surface fatigue processes at impact wear of powder materials, Wear 263 (1–6) (2007) 463–471, https://doi.org/10.1016/j.wear.2006.11.033.
[111] M.H. Chuang, M.H. Tsai, W.R. Wang, S.J. Lin, J.W. Yeh, Microstructure and wear behavior of $Al_xCo_{1.5}CrFeNi_{1.5}Ti_y$ high-entropy alloys, Acta Mater. 59 (16) (2011) 6308–6317, https://doi.org/10.1016/j.actamat.2011.06.041.
[112] Z. Xu, Q.Y. Li, Microstructure, mechanical properties, and wear behavior of AlCoCrFeNi high entropy alloy and AlCrFeNi medium entropy alloy with WC addition, Wear 522 (2023) 204701, https://doi.org/10.1016/j.wear.2023.204701.
[113] H.X. Zhang, J.J. Dai, C.X. Sun, S.Y. Li, Microstructure and wear resistance of TiAlNiSiV high-entropy laser cladding coating on Ti-6Al-4V, J. Mater. Process. Technol. 282 (2020) 116671, https://doi.org/10.1016/j.jmatprotec.2020.116671.
[114] I. Dinaharan, T. Albert, Effect of reinforcement type on microstructural evolution and wear performance of copper matrix composites via powder metallurgy, Mater. Today Commun. 34 (2023) 105250, https://doi.org/10.1016/j.mtcomm.2022.105250.
[115] M.A. Shaik, B.R. Golla, Development of highly wear resistant Cu - Al alloys processed via powder metallurgy, Tribol. Int. 136 (2019) 127–139, https://doi.org/10.1016/j.triboint.2019.03.055.
[116] J. Lee, J.M. Park, J. Moon, H. Park, H.S. Kim, Charpy impact toughness of Cu–Fe–Mn-based immiscible medium-entropy alloys, Mater. Sci. Eng. 862 (2023) 144464, https://doi.org/10.1016/j.msea.2022.144464.
[117] Chongyang Liu, et al., Preparation of graphene film reinforced CoCrFeNiMn high-entropy alloy matrix composites with strength-plasticity synergy via flake powder metallurgy method, J. Mater. Res. Technol. 27 (2023) 7614–7626, https://doi.org/10.1016/j.jmrt.2023.11.182.
[118] Abayomi Adewale Akinwande, M. Saravana Kumar, Tribological performance of a novel 7068-aluminium/lightweight-high-entropy-alloy fabricated via powder metallurgy, Mater. Chem. Phys. 308 (2023) 128207, https://doi.org/10.1016/j.matchemphys.2023.128207.
[119] Ranti Samuel, Oke, Abiodun Bayode, Assessing wear and corrosion in oxide reinforced AlCrFeNi high entropy alloy fabricated via field assisted sintering technique, Mater. Today Commun. 38 (2024) 107734, https://doi.org/10.1016/j.mtcomm.2023.107734.
[120] Mertcan Kafali, Kadir Mert Doleker, Wear, corrosion and oxidation characteristics of consolidated and laser remelted high entropy alloys manufactured via powder metallurgy, Surf. Coating. Technol. 467 (2023) 129704, https://doi.org/10.1016/j.surfcoat.2023.129704.
[121] Priyatosh Pradhan, Yagnesh Shadangi, Powder metallurgical processing of CrMnFeCoMo high entropy alloy: phase evolution, microstructure, thermal stability and mechanical properties, J. Alloys Compd. 935 (2023) 168002, https://doi.org/10.1016/j.jallcom.2022.168002.
[122] Hansung Lee, Ashutosh sharma, Exploring strengthening mechanism of FeCoNiAl high-entropy alloy by non-metallic silicon addition produced via powder metallurgy, J. Alloys Compd. 947 (2023) 169545, https://doi.org/10.1016/j.jallcom.2023.169545.
[123] Li Chen, et al., Microstructure and tensile properties of metastable $Fe_{50}Mn_{30}Co_{10}Cr_{10}$ high-entropy alloy prepared via powder metallurgy, J. Alloys Compd. 955 (2023) 170225, https://doi.org/10.1016/j.jallcom.2023.170225.
[124] Y. Xing, C.J. Li, Strengthening and deformation mechanism of high-strength CrMnFeCoNi high entropy alloy prepared by powder metallurgy, J. Mater. Sci. Technol. 132 (2023) 119–131, https://doi.org/10.1016/j.jmst.2022.06.009.
[125] Jorge Montero, Ek Gustav, Improving the hydrogen cycling properties by Mg addition in Ti-V-Zr-Nb refractory high entropy alloy, Scripta Mater. 194 (2021) 113699, https://doi.org/10.1016/j.scriptamat.2020.113699.
[126] Sheetal kumar dewangan, Vinod Kumar Sharma, Synthesis and characterization of hydrogenated novel AlCrFeMnNiW high entropy alloy, Int. J. Hydrogen Energy 45 (2020) 16984–16991, https://doi.org/10.1016/j.ijhydene.2019.08.113.
[127] G. Zepon, D.R. Leiva, Hydrogen-induced phase transition of $MgZrTiFe_{0.5}Co_{0.5}Ni_{0.5}$ high entropy alloy, Int. J. Hydrogen Energy 43 (2018) 1702–1708, https://doi.org/10.1016/j.ijhydene.2017.11.106.
[128] Sakine Khajavi, Mohammad Rajabi, Effect of cold rolling and ball milling on first hydrogenation of $Ti_{0.5}Zr_{0.5}$ ($Mn_{1-x}Fe_x$) Cr1, x ¼ 0, 0.2, 0.4, J. Alloys Compd. 775 (2019) 912–920, https://doi.org/10.1016/j.jallcom.2018.10.179.
[129] Yanjie Wang, et al., Superior cycle life of TiZrFeMnCrV high entropy alloy for hydrogen storage, Scripta Mater. 212 (2022) 114548, https://doi.org/10.1016/j.scriptamat.2022.114548.
[130] A. Kumar, A. Singh, A. Suhane, Mechanically alloyed high entropy alloys: existing challenges and opportunities, J. Mater. Res. Technol. 17 (2022) 2431–2456, https://doi.org/10.1016/j.jmrt.2022.01.141.